Biophysical Journal
Article

Biophysical Society

Branched actin cortices reconstituted in vesicles sense membrane curvature

Lucia Baldauf,[1] Felix Frey,[1] Marcos Arribas Perez,[1] Timon Idema,[1,*] and Gijsje H. Koenderink[1,*]
[1]Department of Bionanoscience, Kavli Institute of Nanoscience Delft, Delft University of Technology, Delft, the Netherlands

ABSTRACT The actin cortex is a complex cytoskeletal machinery that drives and responds to changes in cell shape. It must generate or adapt to plasma membrane curvature to facilitate diverse functions such as cell division, migration, and phagocytosis. Due to the complex molecular makeup of the actin cortex, it remains unclear whether actin networks are inherently able to sense and generate membrane curvature, or whether they rely on their diverse binding partners to accomplish this. Here, we show that curvature sensing is an inherent capability of branched actin networks nucleated by Arp2/3 and VCA. We develop a robust method to encapsulate actin inside giant unilamellar vesicles (GUVs) and assemble an actin cortex at the inner surface of the GUV membrane. We show that actin forms a uniform and thin cortical layer when present at high concentration and distinct patches associated with negative membrane curvature at low concentration. Serendipitously, we find that the GUV production method also produces dumbbell-shaped GUVs, which we explain using mathematical modeling in terms of membrane hemifusion of nested GUVs. We find that branched actin networks preferentially assemble at the neck of the dumbbells, which possess a micrometer-range convex curvature comparable with the curvature of the actin patches found in spherical GUVs. Minimal branched actin networks can thus sense membrane curvature, which may help mammalian cells to robustly recruit actin to curved membranes to facilitate diverse cellular functions such as cytokinesis and migration.

SIGNIFICANCE Animal cells move, deform, and divide using their actin cortex, a thin layer of filamentous proteins that supports the plasma membrane. For these actions, actin must often assemble at curved sections of the membrane, which is widely believed to require the action of dedicated curvature-sensitive actin- or membrane-binding proteins. Here, we use a bottom-up reconstitution approach to ask whether actin networks are intrinsically able to sense membrane curvature. We show that membrane-nucleated actin cortices can indeed preferentially self-assemble at concave membranes generated by hemifusion of lipid vesicles. This raises intriguing questions about how such curvature recognition works, and whether cells exploit this intrinsic capability of branched actin networks to concentrate actin in specific cortical regions.

INTRODUCTION

The actin cortex is a thin but dense meshwork of cytoskeletal actin filaments that lines the plasma membrane of animal cells. It provides mechanical stability to the cell surface, yet also actively drives cellular shape changes necessary for cell division, cell migration, and tissue morphogenesis. The main structural component of the cortex is filamentous actin. More than 100 actin-binding proteins, including nucleators, membrane-anchoring proteins, crosslinkers, and motors, control the organization, turnover dynamics, thickness, and mechanical properties of the cortical actin meshwork (1). Proteomic and functional studies have shown that cortical actin filaments are nucleated primarily by the formin Dia1 and the Arp2/3 complex (2,3). Dia1 generates linear actin filaments and associates with their fast-growing (barbed) end (4), whereas the Arp2/3 complex binds to the side of a pre-existing actin filament and nucleates a new actin filament from its slow-growing (pointed) end upon activation by a nucleation promoting factor such as N-WASP (5). As a consequence of this mechanism, Arp2/3-mediated actin network growth is autocatalytic and results in branched arrays (6–8).

Cortical actin networks accumulate at various curved plasma membrane structures, for instance in the cytokinetic

Submitted September 1, 2022, and accepted for publication February 14, 2023.

*Correspondence: t.idema@tudelft.nl or g.h.koenderink@tudelft.nl

Lucia Baldauf's present address is London Centre for Nanotechnology, University College London, London, United Kingdom.

Felix Frey's present address is Institute of Science and Technology Austria, Klosterneuburg, Austria.

Lucia Baldauf and Felix Frey contributed equally to this work.

Editor: Kinneret Keren.

https://doi.org/10.1016/j.bpj.2023.02.018

ring (9,10) and tunnel-like wounds (11), in phagocytic cups (12), micropatterned environments (13), and near the nucleus during cell migration in tight spaces (14). However, it remains unknown whether cortical actin networks have any intrinsic ability to sense and respond to membrane curvature. Any such abilities are difficult to observe in living cells, as cortical actin interacts with a multitude of curvature-sensitive actin-binding partners, including membrane-bending BAR-domain proteins (15–18), curvature-sensitive septins (19,20), and IQGAP proteins (21), possibly obscuring any intrinsic curvature sensitivity of the actin network itself. Conversely, it is also unknown how cortical actin affects the generation of membrane curvature. On the one hand, polymerizing actin can generate membrane curvature by exerting pushing forces (22,23), but on the other hand the high rigidity of the cortex may counteract membrane deformation (24,25).

To study how simple actin networks intrinsically interact with curved membranes, we pursue a bottom-up reconstitution approach. Reconstitution of actin inside cell-sized, deformable membrane compartments has been gaining traction recently, with several studies exploring how actin networks self-organize in and shape giant unilamellar vesicles (GUVs) (22,26–33). However, systematic *in vitro* characterization of the interplay between the membrane and a dynamic actin cortex in GUV assays has been challenging due to difficulties with reproducible actin encapsulation.

In principle, various approaches are available for GUV formation, ranging from methods based on swelling dried lipid films (34–41) through picoinjection of droplet-templated GUVs (42,43) to emulsion-based approaches (44–53). However, most of these approaches are incompatible with actin encapsulation, as their yield drops dramatically when encapsulating proteins in physiological buffers. The most successful strategies for reconstituting actin in GUVs have been emulsion-transfer methods, where droplets of protein-containing aqueous solution are formed in an oil phase, stabilized by a self-assembled lipid monolayer, and transformed into GUVs by passing through a second lipid monolayer. One version of this type of GUV preparation is continuous droplet interface crossing encapsulation (cDICE), a method where droplets are created by injecting a continuous stream of inner protein-containing solution into the oil phase by means of a thin glass capillary. The inner aqueous phase is supplemented with a density medium, and the oil phase is placed atop an aqueous subphase inside a rotating chamber, so GUVs can be created on a single compact device (49). Although cDICE has been used for actin encapsulation in several studies (22,26,27,30–32,54,55), recent optimization efforts have made it significantly more robust (56), and attempts at simplifying the method have also been made (53). Nonetheless, the technique remains relatively slow and cumbersome, and a full characterization of the produced GUVs is lacking.

Here, we establish a robust and fast variant of the cDICE method which we term emulsion droplet interface crossing encapsulation (eDICE) to reconstitute biomimetic actin cortices inside GUVs. We show that Arp2/3-mediated assembly generates either cortical actin patches or continuous actin cortices, depending on the concentration of actin and its nucleation factors. Interestingly, these cortical patches are associated with membrane curvature. Serendipitously, we discovered that cortical actin patches recognize membrane curvature because our GUV formation protocol produces a small fraction of dumbbell-shaped GUVs that likely originate from nested GUVs. We use these dumbbell-shaped GUVs as a model system in which the membrane provides a substrate with fixed and spatially varying curvature, and find that actin networks have a strong preference for assembling at regions of concave membrane curvatures on the micrometer-scale.

MATERIALS AND METHODS

Materials

Chemicals

The following chemicals were purchased from Sigma-Aldrich: Tris(hydroxy-methyl)aminomethane hydrochloride (Tris-HCl), potassium chloride (KCl), calcium chloride ($CaCl_2$), magnesium chloride ($MgCl_2$), Optiprep (catalog # D1556-250ML), D-(+)-glucose, DL-dithiothreitol (DTT), adenosine 5′-triphosphate magnesium salt (MgATP), adenosine 5′-triphosphate disodium salt (Na_2ATP), proto-catechuic acid (PCA), proto-catechuate-3,4-dioxygenase (PCD), 3-(N-morpholino)propanesulfonic acid (MOPS), ethylene glycol-bis(β-aminoethyl ether)-tetraacetic acid (EGTA), ethylenediaminetetraacetic acid (EDTA), glycerol, β-casein, silicone oil (5 cSt), light mineral oil (BioReagent), and chloroform (Uvasol). n-Decane (99% pure) was purchased from Arcos Organics. Chloroform, mineral oil, and silicone oil were stored in a glove box with an ambient humidity below 1%.

Lipids

All lipids were purchased from Avanti Polar Lipids: 1,2-dioleoyl-sn-glycero-3-phosphocholine (DOPC), 1,2-distearoyl-sn-glycero-3-phosphoethanolamine-N-[methoxy-(poly-ethylene glycol)-2000] (DOPE-PEG2000), 1,2-dioleoyl-sn-glycero-3-[(N-(5-amino-1-carboxypentyl) iminodiacetic acid) succinyl] (DGS-NTA(Ni)), and 1,2-dioleoyl-sn-glycero-3-phosphoethanolamine-N-(Cyanine 5) (DOPE-Cy5). DOPC was purchased in powder form and dissolved in chloroform to 25 mg/mL, whereas the other lipids were purchased as a solution in chloroform and used as delivered. All lipids were stored in chloroform under argon at −20°C.

Proteins

Rabbit skeletal muscle actin was purchased from Hypermol (catalog # 8101-03). The lyophilized powder was dissolved according to the supplier's instructions, resulting in a solution of monomeric (G-)actin at a concentration of 23.8 μM (= 1 mg/mL) in G-actin storage buffer (2 mM Tris-Cl, pH 8.2, 0.4 mM ATP, 0.1 mM DTT, 0.08 mM $CaCl_2$, and 0.2% unspecified disaccharides). The G-actin solution was left to rest on ice for 2 h and cleared by centrifugation at 148,000 × g for 1 h. Clearing did not result in a measurable loss of protein concentration, as verified by UV absorption measurements at 290 nm using a NanoDrop 2000c spectrophotometer using an extinction coefficient $\varepsilon_{290} = 0.617\ \mathrm{mg/mL}$ (57). Fluorescent G-actin was prepared by labeling G-actin with Alexa Fluor 488 carboxylic acid succimidyl ester (Invitrogen, through Thermo Fisher Scientific, catalog #

A20000) following Ref. (58). Free dye was removed by size exclusion chromatography using a PD MiniTrap G-25 desalting column (cellulose membrane with a 14 kDa molecular weight cut-off, Sigma-Aldrich, catalog # D9527-100FT). The 10×His-tagged VCA-domain of murine N-WASP (amino acids 400–501) was expressed in *Escherichia coli* BL21 (DE3) cells and purified following Ref. (59). It was fluorescently labeled with Alexa Fluor C5 maleimide (Molecular Probes) following the supplier's protocol. Excess dye was removed from the protein by buffer exchange on a PD MiniTrap gravity column with Sephadex G-25 resin. The plasmid was a kind gift from Kristina Ganzinger (AMOLF). Human Arp2/3 isoforms ArpC1B/C5L and ArpC1A/C5 purified from SF21 insect cells were kindly provided by Michael Way (Francis Crick Institute) (60). Arp2/3 was stored at a stock concentration of 1 μM in Arp2/3 storage buffer (20 mM MOPS pH 7.0, 100 mM KCl, 2 mM $MgCl_2$, 5 mM EGTA, 1 mM EDTA, 0.5 mM DTT, 0.2 mM ATP, 5% (v/v) glycerol). Arp2/3 protein complex from porcine brain was purchased from Hypermol EK (catalog # 8413-01). The lyophilized protein was dissolved following the supplier's instructions and stored at 2.23 μM in Arp2/3 storage buffer. SNAP-tagged murine capping protein (CP) was expressed in *E. coli* BL21 Codon Plus (DE3)-RP cells (Agilent Technologies) and purified according to Ref. (61). The plasmid was a kind gift from David Kovar (University of Chicago). After elution from Talon cobalt affinity resin, the protein was dialyzed overnight at 4°C (catalog # D9527-100FT, cellulose membrane with a 14 kDa molecular weight cut-off, Sigma-Aldrich) into CP storage buffer (10 mM Tris-HCl pH 7.5, 40 mM KCl, 0.5 mM DTT). All proteins were snap-frozen and stored in small aliquots at −80°C. G-actin aliquots were thawed quickly and stored on ice for no more than 1 week. Unlabeled and labeled G-actin monomers were mixed in a 10:1 molar ratio for fluorescence imaging. G-actin solutions were left on ice for at least 2 h before use, to allow for depolymerization of any filamentous (F-)actin (62). Thawed aliquots of VCA, Ar2/3, and CP were kept on ice and used within 2 days.

GUV preparation

Buffers

Buffer conditions were kept consistent between all experiments. Unless otherwise specified, the inner aqueous solution (IAS) inside the GUVs contained F-buffer (20 mM Tris-HCl pH 7.4, 50 mM KCl, 2 mM $MgCl_2$, 1 mM DTT, 0.5 mM MgATP) supplemented with 0.5 μM PCD and 10 mM PCA to minimize photobleaching (63), as well as 6.5% V/V Optiprep to increase the mass density. We reduced the Optiprep concentration compared with the cDICE method (56) as we found that it substantially affects actin polymerization kinetics, whereas eDICE production of GUVs is effective over a range of Optiprep concentrations (Fig. S13). The IAS osmolarity was 168 mOsm/kg in all experiments and was unchanged by the addition of proteins, as measured using a freezing point osmometer (Osmomat 010, Gonotec, Germany). The outer aqueous solution (OAS), in which the GUVs were first produced, contained 190 mM glucose (200 mOsm/kg). Immediately after GUV formation, we added a solution of 40 mM Tris-HCl pH 7.4 and 90 mM glucose (182 mOsm/kg), to stabilize the pH outside the GUVs and reach final buffer conditions of 10 mM Tris-HCl pH 7.4 and 170 mM glucose, with an osmolarity of 189 mOsm/kg to slightly deflate the GUVs and increase the available excess membrane area by an average of 7.6% (64).

Lipid-in-oil solution

Lipid stocks were prepared in chloroform solution. DOPC (94.985%) was mixed with 0.01% DOPE-PEG2000 to increase GUV yield following (56), 5% DGS-NTA(Ni) to recruit VCA, and 0.005% DOPE-Cy5 for fluorescent visualization (molar percentages). Mixtures with a total lipid content of 1.7 μmol were dried under a gentle N_2 stream in a screw-cap glass vial for each experiment and used within a day. This yields a final lipid concentration of $\sim$ 0.25 mmol/L in the oil phase. The vials with dried lipid films were then transferred into a glovebox under an inert environment containing <1% environmental humidity, to promote a reproducible and high yield of GUVs (56). In the glovebox, silicone oil and mineral oil were combined in a volumetric ratio of 5.3:1.2 and thoroughly mixed by vortexing. Dried lipid films were dissolved either in 415 μL of chloroform or they were dissolved in 50 μL of chloroform and subsequently diluted with 400 μL of n-decane. Under continuous gentle vortexing, 6.5 mL of the oil mix was slowly added to each lipid vial. The vials were sealed tightly with Teflon tape and parafilm, removed from the glove box, and sonicated on ice in a bath sonicator for 15 min. The lipid-in-oil solutions were stored on ice and used for GUV formation within 30 min.

GUV formation and handling

GUV preparation and imaging were performed at room temperature (24°C $\pm$ 1°C). We used a home-built spinning chamber setup equipped with a spinning table and 3D-printed chamber described in Ref. (56) to prepare GUVs. We first set the spinning chamber to rotate at 2000 rpm (corresponding to a motor voltage of 14.5 V on our device), added 700 μL of OAS, and carefully layered on 5 mL of the oil solution. Then 1 mL of oil solution was set aside in a 2-mL Eppendorf tube. We then created droplets of IAS in the 1 mL oil solution by manual emulsification: 25 μL of IAS were prepared on ice, adding G-actin last. The IAS was then pipetted into the 1 mL of oil solution and emulsified by scratching the Eppendorf tube vigorously over an Eppendorf holder 14 times. This simple procedure allows us to form droplets within < 15 s. Note that a recent work has shown that droplets can also be prepared by vigorous pipetting (53). The emulsion was immediately pipetted into the spinning chamber and centrifuged for 3 min to form GUVs.

After GUV formation, the spinning chamber was stopped by slowly turning down the motor voltage, and excess oil was removed by careful pipetting. Then 233 μL of outer buffer were added to the remaining aqueous phase to stabilize the OAS pH, and the GUVs were concentrated by resting the spinning chamber at a 45° angle for 10 min. GUVs were retrieved using a cut-off 200 μL pipet tip to minimize shear forces during transfer. The samples were finally diluted threefold in imaging buffer (10 mM Tris-HCl pH 7.4, 165 mM glucose).

Microscopy

Image acquisition

GUVs were observed either in ibidi 18-well μ-slides (catalog # 81817) or in chambers created by mounting silicone spacers (Sigma-Aldrich, catalog # GBL665106) on # 1.5 coverslips (Superior Marienfeld, catalog # 0107222). To prevent adhesion of the GUVs, the wells were passivated by incubating with a 0.1-mg/mL β-casein solution in 10 mM Tris-HCl pH 7.4 for at least 15 min, rinsed with MilliQ water, and dried under N_2 flow. After GUV addition, we closed the chambers to prevent solvent evaporation and keep the osmotic deflation of the GUVs constant. Ibidi wells were closed with the appropriate lid, which effectively prevents evaporation over several days. Chambers made from silicone spacers were sealed from the top with a glass coverslip and affixed to the spacer with vacuum grease (Dow Corning high-vacuum silicone grease, Sigma-Aldrich catalog # Z273554). Confocal images were acquired either on an inverted Olympus IX81 confocal spinning disk microscope equipped with 491- and 640-nm continuous wave lasers, a 100× oil immersion objective (UPlanSApo, WD 0.13 mm, NA 1.4) and an EM-CCD Andor iXon X3 DU897 camera, or on an inverted Leica Stellaris 8 laser scanning confocal microscope equipped with a white light laser, a 63× glycerol immersion objective (HC PL APO, WD 0.3 mm, NA 1.2), and HyD S and HyD X detector operated in photon counting mode. Z stacks were acquired with a 1 μm step height unless otherwise specified. Further imaging settings are listed in Table S1.

Quantitative confocal microscopy

Quantitative confocal microscopy to determine the actin encapsulation efficiency in GUVs was performed on the Leica Stellaris 8 LSCM using the 63× glycerol immersion objective and the HyD S detector operated in

counting mode. We performed all measurements in 1 day and in a single ibidi 18-well μ-slide to avoid artifacts from variations in coverslip thickness. To ensure that images were always taken at the same height above the coverslip surface, we first acquired a 256 $\times$ 256 pixel xz-image (Fig. S4 *A*). We subsequently acquired an image of 2048 $\times$ 2048 pixels 7 μm above the coverslip surface (Fig. S4 *B*). For each GUV sample, we acquired at least 10 fields of view, corresponding to > 1000 GUVs per condition. To convert fluorescence intensity to absolute actin concentrations, we obtained calibration data by imaging bulk F-actin solutions at a range of concentrations under identical imaging conditions (Fig. S4 *H* and *I*).

Fluorescence recovery after photobleaching experiments

Fluorescence recovery after photobleaching (FRAP) experiments to determine membrane continuity for dumbbell-shaped GUVs were performed on the Leica Stellaris 8 LSCM with a 63$\times$ glycerol immersion objective. GUV membranes were labeled with 0.05% mol/mol DOPE-Cy5. We imaged the equatorial section of dumbbell GUVs at high zoom (typically 9$\times$) and with a 512 $\times$ 512-pixel field of view. The white light laser was operated at 658 nm and at 8% laser power with a pixel dwell time of 0.95 μs during acquisition of the pre- and post-bleach images. Bleaching was performed on a rectangular region of interest (ROI), which encompassed the bright lobe of a dumbbell and was thus different in size and aspect ratio for each vesicle. The ROI was bleached using four laser lines (643, 648, 653, and 658 nm) operated at 100% intensity each, to efficiently bleach the membrane within a single frame (= 249 ms). We acquired three images before bleaching the GUV at four frames per second (4 fps). After bleaching, we acquired 50 frames at 4 fps, followed by another 50 frames at 2 fps, to capture membrane dynamics for 38 s.

Since dumbbell GUVs were in suspension and hence freely diffused during the course of imaging, we extracted line profiles for each frame individually, tracing the dumbbell membrane around first the bright and then the dim lobe, using the ImageJ plot-profile function (65). Time-dependent intensity ratios I_{bright}/I_{dim} were extracted from the profiles using a custom-written python script.

Image analysis

Analysis of vesicle sizes

Vesicle sizes were measured by acquiring a confocal z stack of each GUV and fitting a circle to the equatorial slice using ImageJ (65). We analyzed a total of 494 GUVs from four separate experiments.

Quantitative analysis of actin encapsulation in GUVs

Quantitative confocal microscopy images were analyzed in an automated procedure. First, we located GUVs in the membrane images using the template-matching module in the open source DisGUVery toolbox (66) (see Fig. S4 *C*). The images were preprocessed by smoothing with a filter size of 15 and edge enhancement with a filter size of 45. A representative image of a GUV membrane was used as a template, and matches with a matching index of above 0.4 were detected with 40 size steps ranging from 0.3 to 2 times the template size. Since membrane labeling was deliberately kept low to avoid any spectral crosstalk artifacts, we could only detect 30%–60% of GUVs in any given image, but we observed no systematic bias in which GUVs were detected or missed. Next, we extracted the average actin fluorescence in the GUVs with a custom python script. We created a circular ROI of radius $R = d_{bb}/2$, where d_{bb} is the size of the bounding box detected by the template matching GUV detection (Fig. S4 *D* and *E*). We then extracted the pixel intensities for the actin signal within the ROI and averaged these over the ROI for each GUV (Fig. S4 *F*). Resulting intensity distributions were converted to actin concentrations by means of a calibration curve determined for bulk actin networks (Fig. S4 *H* and *I*). For these bulk networks, we averaged the mean pixel intensity in at least five images of 2048 $\times$ 2048 pixels per condition. A proportional fit of measured actin signal versus nominal actin concentration in the form $I_{act}(c_{act}) = A \cdot c_{act}$ was computed using numpy least-squares fitting, and the resulting proportionality constant was used to convert actin intensity in GUVs into actin concentrations.

Classification of actin cortex phenotypes

Cortex phenotypes for each GUV were categorized manually from confocal z stacks in one of four categories: in "inside patch," GUV has one or more actin patches in the lumen; in "concave patch," GUV has one or more actin patches that visibly protrude into the GUV lumen and/or colocalize with a section of membrane that is locally bent inward; in "flat patch," GUV has one or more actin patches on the membrane, which do not colocalize to a concave actin patch and do not encompass the entire GUV; in "continuous cortex," GUV has an enhanced actin signal on the membrane compared with the lumen throughout the membrane. Dumbbell-shaped GUVs were excluded from the analysis of all GUVs and considered separately (below).

Dumbbell GUV shape analysis

The size and shape of dumbbell GUVs were extracted manually from confocal z stacks using ImageJ (65). We fitted circular ROIs to each lobe in the equatorial slice of the dumbbell and measured the lobe diameters. We then drew a line profile across the neck of the dumbbell and extracted the distance between the two peaks in membrane signal on either side of the neck opening. Geometric features of the dumbbells (bright-to-dark size ratio, average lobe diameter, neck-to-lobe ratio) were computed from the lobe sizes and neck diameters in python.

Classification of actin localization on dumbbell GUVs

Actin localization in dumbbell necks was classified manually in confocal z stacks acquired on the Stellaris 8 LCSM. The dumbbell vesicles were first visually inspected to assess whether there was visible local actin enrichment anywhere on the membrane. It was further noted whether enrichment occurred in the neck region. If so, a maximum intensity projection of the GUV was generated in ImageJ (65). On the basis of visual inspection of the projection, we classified the GUV as possessing one or more than one actin patch at the neck (single patch or multi patch), or enrichment in the entire neck region (continuous enrichment).

Quantification of membrane curvatures

Membrane curvatures in concave actin patches in spherical GUVs containing CP or around dumbbell necks were assessed using the ImageJ plugin Kappa - Curvature analysis (version 2.0.0) (67). For each curved membrane region, we drew a 5-pixels-wide ROI around the relevant membrane section (typically 5–10 μm long), and used Kappa to extract the membrane curvature in the $x - y$ plane in this region, based on B-splines fit to the membrane contour. The full curves were exported to a custom python script, to compute the signed curvature κ_1 in the $x - y$-plane. The surface curvature was calculated as $\kappa = \kappa_1 + \kappa_2$, where κ_2 is the curvature in the orthogonal direction along the membrane. For actin patches on spherical GUVs, we assumed $\kappa_1 = \kappa_2$ to reflect a rotationally symmetric actin patch. For dumbbell necks, κ_2 was calculated from the dumbbell's neck diameter d_{neck} as $\kappa_2 = (d_{neck}/2)^{-1}$. Note that the two curvatures have the same sign in concave patches, but opposite signs in the neck. We further note that the curvatures measured here are limited by the resolution of confocal fluorescence microscopy, as well as by the segmentation. Local curvatures, particularly at the dumbbell neck, may be significantly higher than we can measure with optical methods.

Quantification of actin localization

Actin localization at membrane necks was quantified using fluorescence line profiles extracted in ImageJ. We compared intensities in two line profiles, one through the ROI (i.e., across the dumbbell neck) and one reference region (i.e., a line along the rotational symmetry axis of the dumbbell). Line profiles of width 8 pixels were extracted in ImageJ and exported to a custom

python script to determine the degree of enrichment as the ratio between the maximum actin intensity in the neck region, divided by the maximum actin intensity in the reference region.

RESULTS

A robust protocol for actin encapsulation

To study the interactions between cortical actin and lipid bilayer membranes, we reconstituted membrane-anchored actin cortices inside GUVs. We used a modified emulsion-transfer method adapted from a recently optimized cDICE procedure (56) (Fig. 1 *A*). We used the same optimized spinning chamber setup reported in (56) and took care to maintain low-humidity conditions during the procedure to enhance the GUV yield. However, rather than forming the droplets by injection of the IAS through a capillary, we pipetted pre-formed emulsion droplets into the spinning chamber. Using pre-formed droplets has several important advantages. First, it avoids problems that can arise from clogging of the capillary needed to produce droplets with cDICE. Second, it speeds up the encapsulation step, reducing the time during which the G-actin monomers are at room temperature from several minutes to under 15 s, hence preventing premature actin polymerization (68). Third, it allows downscaling of the amount of IAS required to generate samples from >100 μL for cDICE to <30 μL in the case of eDICE, which is important when working with recombinant proteins available only in small amounts. eDICE robustly produced a high number of GUVs that were polydisperse in size and in encapsulated protein concentration. In addition to the GUVs, of which a small fraction typically had one or more small lipid pockets attached, we also usually found some large lipid aggregates (bright cyan spots in Fig. 1 *B*) that were not physically attached to GUVs. The average GUV size (9 μm) was comparable with that obtained with optimized cDICE (12 μm (56)), and reproducible across independent experiments (Fig. 1 *C*).

To quantify the encapsulation efficiency, we analyzed confocal fluorescence images of actin inside the GUVs and converted intensities to concentrations using calibration measurements on bulk actin solutions. We found that the mean actin concentration inside the GUVs increased linearly with the concentration of actin in the IAS and that the mean value was close to the nominal (input) actin concentration (Fig. 1 *D*). However, the distribution of actin concentrations broadened as the nominal actin concentration increased. Interestingly, at high actin concentrations ($c_{\mathrm{nominal}} \geq 8$ μM), a substantial fraction of the GUVs was supersaturated with actin, containing up to 1.7× the nominal actin concentration, whereas a small fraction of the GUVs showed no measurable actin content at all (Fig. 1 *E*). At low concentrations of actin in the IAS ($c_{\mathrm{nominal}} \leq 2$ μM)), a large fraction of GUVs contained substantially less actin than expected (Fig. 1 *E*). Extended quantification of these results is shown in Fig. S5. Although it is widely known that GUV formation yields a polydispersity in solute concentrations, our results highlight that this polydispersity is in fact nontrivially dependent on the initial solute concentration.

Actin cortex formation proceeds by nucleation and fusion of patches

To form a membrane-nucleated actin cortex, we encapsulated actin along with the nucleating protein Arp2/3 and the Arp2/3-activating protein fragment VCA (Fig. 2 *A*). Nucleation was constrained to the membrane by using a 10×His tag on the VCA protein to recruit it to the GUV membrane via Ni-NTA lipids present at a small density within the membrane.

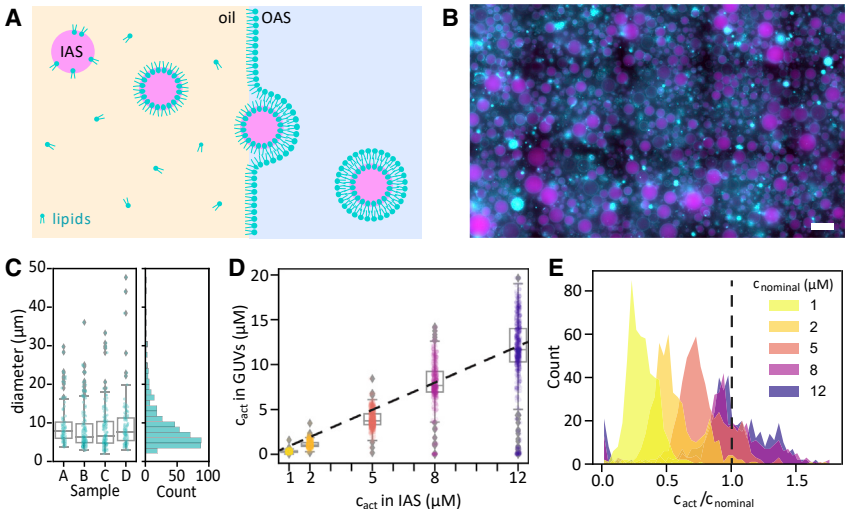

FIGURE 1 Robust actin encapsulation by eDICE. (*A*) Schematic of the eDICE process. Pre-formed lipid-stabilized emulsion droplets containing the inner aqueous solution (IAS) with G-actin are injected into a spinning chamber. Centrifugal forces created by rotation of the spinning chamber establish concentric layers of the oil phase and an outer aqueous solution (OAS) and push the droplets through the oil/OAS interface, where they acquire a second lipid leaflet and thus transform into GUVs. (*B*) Typical widefield image of GUVs formed by eDICE. F-actin is shown in magenta, lipids in cyan. Scale bar, 50 μm. (*C*) Diameter distributions of GUVs from four independent experiments (left) and the aggregated histogram of GUV sizes (right). N per sample: 98, 149, 137, 110. (*D*) Actin concentrations in eDICE GUVs measured by quantitative fluorescence microscopy, as a function of the nominal actin concentration in the IAS. Individual data points indicate single GUVs, boxplots indicate medians and quartiles. (*E*) Histogram of encapsulation efficiency, $c_{\mathrm{rel}} = c_{\mathrm{act}}/c_{\mathrm{nominal}}$, for different nominal actin concentrations. The dashed line represents $c_{\mathrm{rel}} = 1$. $N_c = 515, 468, 536, 368$, and 447 GUVs for $c = 1, 2, 5, 8$, and 12 μM actin, respectively.

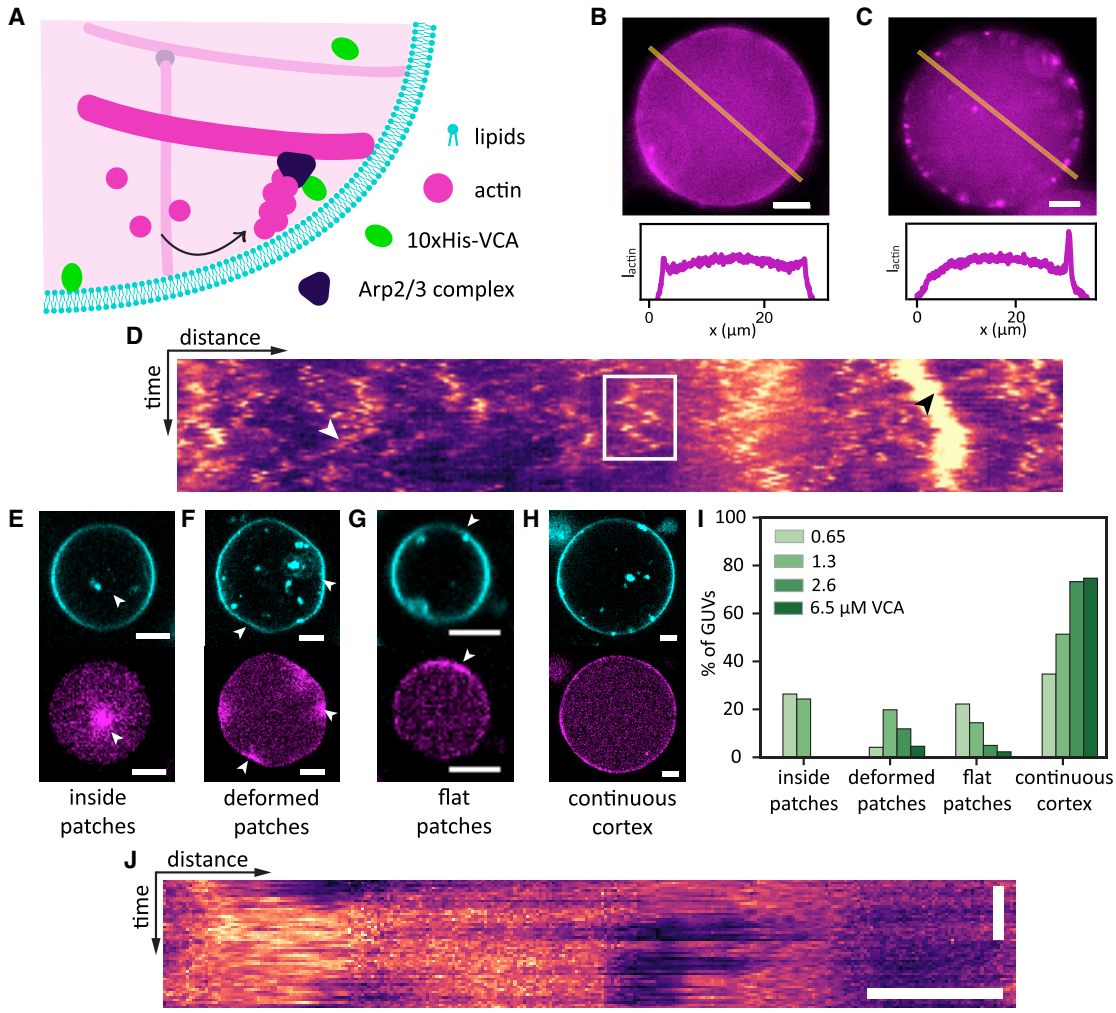

FIGURE 2 Formation of membrane-nucleated actin cortices inside GUVs. (*A*) Actin filaments (magenta) were nucleated using the Arp2/3 complex, which was activated near the inner leaflet of the GUV membrane (cyan) by membrane-bound VCA (green). (*B* and *C*) Top row: at low actin concentration (4.4 μM), actin formed either a continuous cortex (*B*), or small bright patches (*C*), or a combination of both. Bottom row: line profiles of actin fluorescence intensity along the yellow lines in the epifluorescence images. (*D*) Kymograph of a patchy actin cortex from a line drawn along the circumference of a GUV in a time lapse of 50 frames recorded at a frame rate of 1 fps. Scale bars, 10 μm (horizontal), 20 s (vertical). Actin patches could diffuse along the cortex (*white rectangle*), split (*white arrow*), or merge (*black arrow*). (*E*–*H*) At high actin concentration (8 μM), we found bright actin foci inside the lumen (*E*, *white arrow*), bright deformed actin patches (*F*, *white arrows*), extended flat membrane patches (*G*, *white arrow*), or a continuous flat cortex (*H*). All examples show GUVs with 2 μM VCA and 50 nM Arp2/3. Lipids are shown in cyan, actin in magenta. Scale bars, 5 μm. (*I*) Quantification of cortical phenotypes for 8 μM actin and 50 nM Arp2/3 as a function of the density of VCA activator. Actin patches in the GUV lumen occurred only at low VCA concentrations, deformed patches were most prevalent at intermediate VCA concentrations, and continuous cortices were most prevalent at high VCA concentrations. GUVs were all produced on the same day and statistics are based on $N = 72$, 111, 101, and 87 GUVs for VCA concentrations of 0.65, 1.3, 2.6 and 6.5 μM, respectively. (*J*) Kymograph of an actin cortex (8 μM actin) with large flat patches that were immobile. Scale bars, 5 μm (horizontal), 20 s (vertical).

At low actin concentrations (4.4 μM), actin cortices formed with 50 nM Arp2/3 and 0.65 μM VCA exhibited three distinct types of structures. Cortices were either continuous, being enriched all around the GUV (Fig. 2 *B*), or they were made up of distinct small (1–2 μm) cortical actin patches (Fig. 2 *C*), or a combination of both. We note that the prevalence of the three cortex phenotypes varied from day to day, likely due to variations in protein encapsulation efficiency. Kymographs of the actin signal along the membrane (Fig. 2 *D*) revealed that actin patches diffused over the inner vesicle surface on a timescale of seconds (Fig. 2 *D*, white rectangle) and could also split (Fig. 2 *D*, white arrow) or merge (Fig. 2 *D*, black arrow).

When we increased the nominal actin concentration to 8 μM, observations varied much less from day to day.

Furthermore, we no longer found any GUVs with small cortical actin patches. Instead, we observed four different cortical phenotypes whose prevalence varied with VCA concentration. Actin either formed bright patches inside the GUV lumen (Fig. 2 *E*), or patches that were localized to deformed sections of the membrane (Fig. 2 *F*), or large flat patches of cortical actin (Fig. 2 *G*), or continuous actin cortices (Fig. 2 *H*). To test the role of the nucleator density, we varied the VCA concentration, which determines both the rate of actin nucleation and the interaction strength of actin with the membrane, between 0.65 and 6.5 μM while maintaining a constant actin concentration of 8 μM (Fig. 2 *I*). Bright foci in the GUV lumen arose in $\sim$ 23% of GUVs with 0.65 or 1.3 μM VCA, and in a few cases at 2 μM (example in Fig. 2 *E*), whereas actin was always localized at the cortex at higher VCA concentrations. The cortical patches were immobile over a 50 s timespan (kymograph in Fig. 2 *J*), in contrast to the small mobile patches formed at 4.4 μM actin. Flat patches strongly declined in frequency from 22% to 2% of GUVs when the VCA concentration was raised from 0.65 to 6.5 μM, whereas the fraction of GUVs with a continuous cortex rose from 35% to 75% over this VCA concentration range (Fig. 2 *I*). Since patches tend to become larger compared with the GUV perimeter as VCA concentration increases, we eventually classify them as a continuous cortex. Deformed patches were observed both in the presence and absence of a continuous cortex. Their prevalence peaked at a 1.3 μM VCA concentration and dropped to around 4% of GUVs at both ends of the studied VCA concentration range. Note that both flat and deformed patches signify a significant deviation from the curved membrane of a spherical GUV.

eDICE produces some dumbbell-shaped GUVs due to membrane hemifusion

In all GUV samples produced by eDICE, we found some GUVs with a striking dumbbell shape (Fig. 3 *A*). The prevalence of such dumbbell-shaped GUVs varied from experiment to experiment, but they usually made up a few percent of all observed GUVs. These GUVs consisted of two spherical caps connected by an open neck. They could be easily distinguished from GUV doublets, created when two vesicles stick to one another (Fig. 3 *B*), by the fact that they lack a membrane septum. Strikingly, one lobe of the dumbbell appeared as a normal unilamellar vesicle membrane (left lobe in Fig. 3 *A*), whereas the other appeared either as one bright membrane (right lobe in Fig. 3 *A*) or as two separate membranes (Fig. 3 *C*), which could be close together (left panel) or, in rare cases (three out of 85 dumbbells), far apart (right panel). Line intensity profiles along the membrane contours revealed that the brighter lobe showed on average twice the membrane intensity of the dimmer lobe (Fig. 3 *D* and *E*). Thus, dumbbell-shaped GUVs appeared to be made up of one lipid bilayer on the dim side and two on the bright side, consistent with the observation of dumbbells with two well-separated membranes in the bright lobe (Fig. 3 *C*).

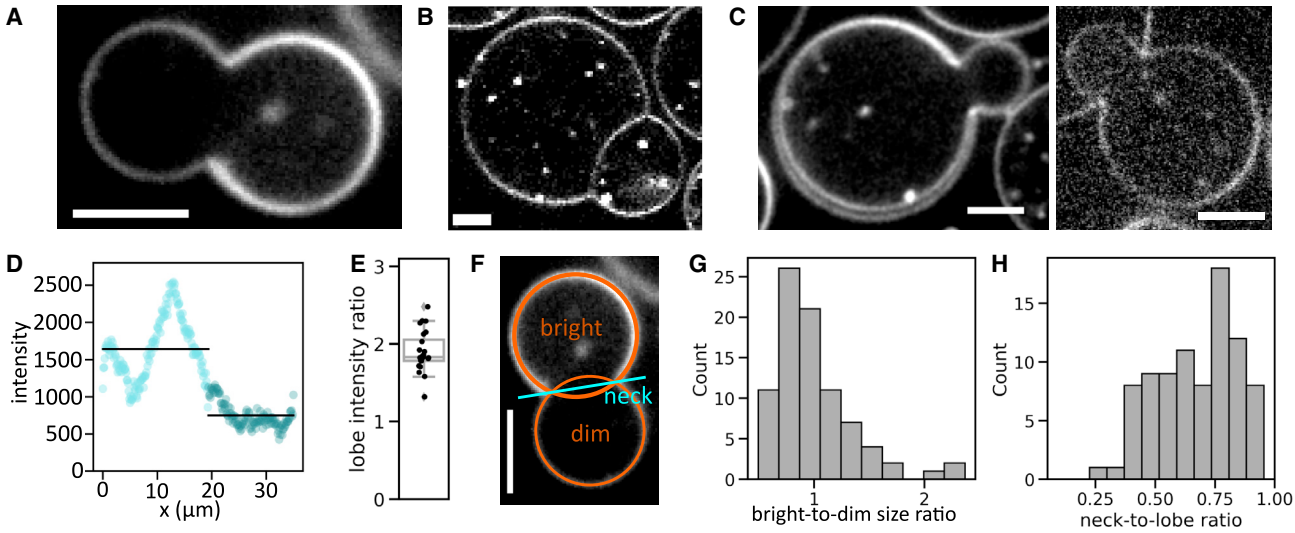

FIGURE 3 Dumbbell-shaped GUVs formed by eDICE. (*A*) Dumbbell-shaped GUV with a bright and a dim spherical cap connected by an open membrane neck. (*B*) GUV doublets clearly look different, exhibiting a membrane septum between the two lobes that each have equal membrane intensity. (*C*) Some dumbbells showed two clearly separate membranes in (parts of) the bright half of the dumbbell with a narrow (left) or wide (right) gap. (*D*) Membrane signal in a 5-pixel-wide line, starting at the neck and following clockwise along the GUV membrane shown in (*A*). Light cyan data points denote the bright half of the GUV; dark cyan data points show the dimmer half. The average signal is 1.8-fold higher (2.1-fold after background subtraction) in the bright than in the dim lobe (*black lines*). (*E*) Boxplot of membrane intensity ratios after background subtraction. The average ratio is 1.9 ($N = 25$ dumbbells from five independent experiments). (*F*) We measured morphological features of GUV dumbbells by fitting circles to their bright and dim lobes (*orange circles*) and measuring the neck diameter as the distance between the maxima in membrane fluorescence in a line profile drawn through the neck. (*G*) Histogram of the size ratio between bright and dim dumbbell lobes ($N = 85$). (*H*) Corresponding histogram of neck-to-lobe size ratios ($N = 85$). Scale bars, 5 μm.

We characterized the shapes of dumbbell vesicles by fitting circles to both lobes in the equatorial plane and measuring the distance between the two membranes at the neck (Fig. 3 *F*). When the two membranes of the bright lobe were visibly separated as in the example in Fig. 3 *C*, we defined the bright lobe size as that of the inner membrane. This analysis revealed that dumbbell shapes were diverse but followed general overall trends. First, the two lobes were usually similar in size, with the dim lobe being slightly larger than the bright lobe in most GUVs (64% of $N = 85$ GUVs), although there were occasional outliers where the bright lobe was more than twice the size of the dim lobe (Figs. 3 *G* and S6). The neck diameter was usually quite wide, ranging from 0.4 to 0.9 times the average lobe diameter (Fig. 3 *H*). Only ∼5% of dumbbells had a neck narrower than 0.4 times the average lobe size.

How could these dumbbell-shaped GUVs arise? Motivated by the observation that a small fraction of GUVs contain another GUV within their lumen (Figs. 4 *A* and S1 *A*), we hypothesized that dumbbells might originate from bursting of such enclosed GUVs. After the inner vesicle leaks its volume into the GUV (Fig. S1 *B*), its bilayer makes contact with the lipid bilayer of the outside GUV (Fig. S1 *C*). Next, the two lipid bilayers merge via hemifusion (Fig. S1 *D*). In this way, a GUV is created with two lobes: in the first lobe, the GUV bilayer membrane is supported by the bilayer of the inner vesicle, whereas, in the second lobe, the GUV bilayer remains alone (Figs. 4 *B* and S1 *E*). Due to diffusion, the lipids within the same membrane leaflet mix (Fig. S1 *E*). How exactly this happens remains unclear, but we suspect that residual oil in the membrane may promote the formation of membrane defects and facilitate membrane fusion. This process should create an interface between the single- and double-bilayer membrane that is associated with a line tension, which is expected to drive the formation of a dumbbell shape (Fig. 4 *B*). Since two of the membrane leaflets of the bright lobe should be disconnected from the two leaflets that envelop the whole dumbbell (Fig. 4 *C*, detailed illustration in Fig. S7 *C*), we can test this interpretation by FRAP. Note that this double layer really comprises only one continuous leaflet, but it is bent in on itself such that it appears as two layers (illustrated in Fig. S7 *C*). The ratio between the average membrane intensities in the bright and the dim lobe should be 2 before bleaching, drop to 0 when we completely photobleach the bright lobe, and return to 1 over time, as the outer leaflets of the bright lobe are replenished by fluorescent lipids from the dim lobe, whereas the disconnected leaflets in the bright lobe remain bleached (Fig. S7 *D*). By contrast, if the leaflets in the two lobes were either fully connected or fully disconnected from one another, the final intensity ratio would be 2 or 0, respectively. Since lipids diffused rapidly in the membrane and recovered after photobleaching within less than 3 s (Fig. S8 *A* and *B*), we could not

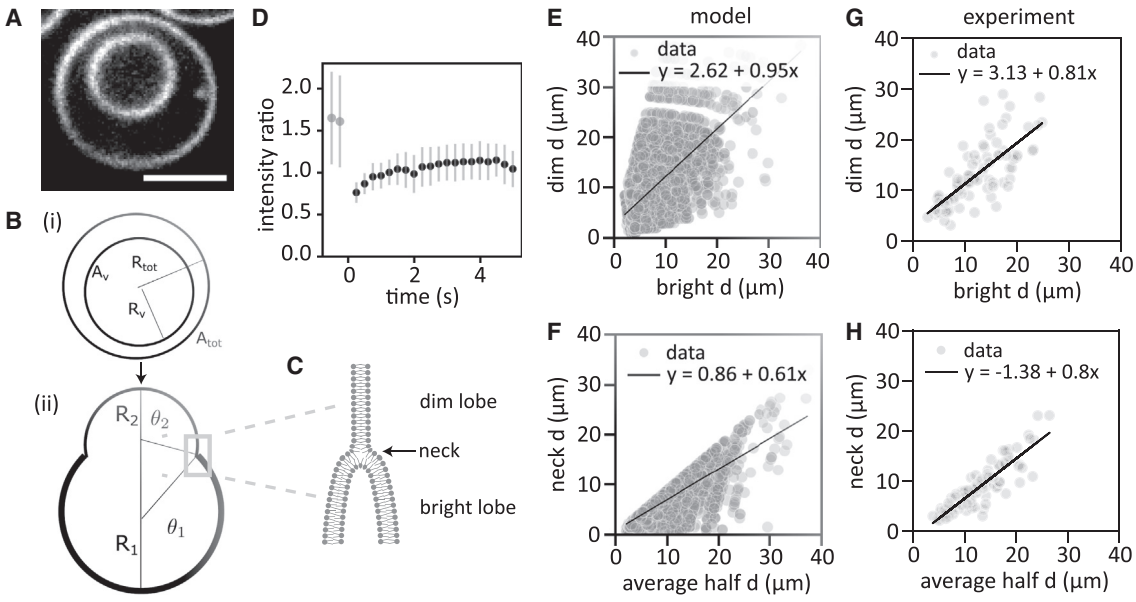

FIGURE 4 Dumbbell shapes result from hemifusion and are determined by osmotic pressure and line tension. (*A*) Confocal image of an eDICE GUV encapsulating another GUV (scale bar, 5 µm). Such nested GUVs were rare (∼5%–10% of GUVs) but present at frequencies comparable with dumbbells. (*B*) Proposed mechanism for dumbbell formation. (i) One vesicle with radius R_{tot} encapsulates another vesicle with radius R_v. (ii) The inner GUV bursts and hemifuses with the membrane of the outer GUV. The shape of the resulting dumbbell is determined by membrane tension and line tension along the hemifusion line. (*C*) Proposed microscopic configuration of the dumbbell neck (gray rectangle in *B*), where one inner and one outer leaflet (*dim lobe*, top) join four concentric leaflets in the bright lobe (bottom). (*D*) FRAP measurement of the bright lobe of a dumbbell reveals a recovery of the normalized fluorescence intensity from ∼2 (pre-bleach, $t < 0$) to ∼1 (post-bleach, $t > 0$) within seconds. (*E* and *F*) The model predicted dumbbell shapes (relative lobe sizes, *E*, and neck diameters relative to the average lobe diameters, *F*) that quantitatively match the experimental data (*G* and *H*). Experimental and simulated data represent $N = 85$ and $N = 10^4$ dumbbell GUVs, respectively. Lines display linear fits (see legend for fit equations).

completely bleach the bright lobe to zero while retaining enough membrane intensity in the dim lobe for data analysis. We could, however, reduce the bright lobe fluorescence to around 30% of its initial value. We found that the lobe intensity ratio recovered within a few seconds and indeed reached a final value that was just over half of its initial value (Fig. 4 *D* and additional data in Fig. S8 *A*), confirming that the lobes were hemifused.

To further test whether a model based on hemifusion of nested GUVs explains the formation of dumbbells, we asked whether the dumbbell geometries were also quantitatively consistent with the geometries expected based on a simple membrane model. We assumed that a GUV of radius R_{tot} encapsulates another vesicle of radius R_v (Fig. 4 *B* (i)). After the encapsulated vesicle bursts, we expect its membrane to stick to that of the outer vesicle. As the membrane area of the inner vesicle is smaller than that of the outer one, this process will inevitably create two regions, one with a single and another with a double membrane. The regions will therefore have different surface tensions, and experience a line tension at their boundary. We can account for these differences in a simple energy model (see section I of the supporting material), from which we find that dumbbell shapes are indeed equilibrium solutions. Unsurprisingly, we found that the surface tensions are related to the osmotic pressure difference across the membrane according to Laplace's law (Eq. S5 in supporting material). Moreover, we found that the overall shape of the dumbbell GUVs is the result of the interplay between this osmotic pressure, which promotes spherical shapes, and the line tension, which tends to constrict the boundary between the two lobes (Eq. S7 in supporting material). Indeed, similar dumbbell shapes have been observed and theoretically predicted in the case of GUVs made of phase-separating lipid mixtures, where line tension along the domain boundary also produces spherical cap shapes (69–72).

To verify the model, we used it to predict the distribution of dumbbell shapes, based on the observed distribution of (spherical) GUV sizes (Fig. 1 *C*). From the model, we can then calculate the ratio of the line tension to the osmotic pressure, as the physical parameter that sets the dumbbell shape. This value, which is difficult to measure directly, can thus be inferred from easily observable quantities such as the lobe and neck radii.

In the model, the total membrane area (the surface area plus excess membrane area) of the bursting vesicle A_v equals the surface area of the double bilayer membrane lobe A_1; i.e., $A_v = A_1$. Moreover, the GUV's total membrane area A_{tot} minus the surface area of the bursting lobe A_1 equals the surface area of the single bilayer membrane lobe A_2; i.e., $A_{tot} - A_1 = A_2$ (Fig. 4 *B* (ii)). Therefore, we related the shape of the dumbbell GUV, given by R_1, R_2, θ_1 and θ_2, i.e., the radii and opening angles of the bright and dim lobe, to the GUV volume and the membrane area of the GUV and the bursting vesicle (for details see section II in the supporting material).

To determine the shapes of dumbbell GUVs, we sampled 10,000 radii R_{tot} and R_v and only recorded values of R_1 and R_2 that were in the experimental range ($< 25\ \mu$m) and corresponded to a defined dumbbell shape ($\pi/2 < \theta_1, \theta_2 < \pi$) with the smallest possible neck radius (i.e., minimal line tension energy). To reduce the number of free parameters in our model, we assumed that both the GUV and the enclosed vesicle have been created with the same reduced area; i.e., $\nu_{tot} = \nu_v = \nu$. To determine the reduced area ν, we matched the simulated data to the experimental data. For $\nu = 1$, no vesicle shape transformations are possible. Hence, we started with $\nu = 1.01$ and increased ν in steps of 0.01 until we reached $\nu = 1.1$. We found the best agreement for a reduced area of $\nu = 1.05$ between the slope and $y-$ intercept of linear fits of the simulated data (Figs. 4 *E* and *F*) and the experimental data (Figs. 4 *G* and *H*).

We found good agreement between bright and dim lobe diameters for the model and the experimental data (Figs. 4 *E* and *G*). The same holds for the relation between the neck diameters and average lobe diameters (Figs. 4 *F* and *H*). The slopes of the linear fits to the experimental and simulation data match nearly quantitatively, with slopes of 0.81 and 0.95 relating the dim and bright lobe diameters, and 0.8 and 0.61 relating the neck diameter and average lobe size. Moreover, the spread in the simulated data is similar to that of the experimental data.

The offset between the experimental and simulated data is likely an artifact of the way in which we select the size of the inner vesicle in the model: we choose a size from the same distribution as the outer GUV size. However, it is currently unclear how the inner vesicles actually form. It is therefore possible that the typical difference in total membrane area between inner and outer GUV is correlated in the experiments, thus resulting in an offset between the experimental and simulated data.

Based on the good agreement of the experimentally observed shapes with a model where line tension drives dumbbell formation, we concluded that membrane hemifusion is indeed sufficient to drive the formation of dumbbell GUVs. This conclusion was supported by the observation that the same geometrical correlations arose whether or not any actin was encapsulated in the GUVs (Fig. S9 *A* and *B*). The conclusion that membrane properties alone are sufficient to form dumbbell GUVs was further confirmed by the fact that they occur in eDICE GUVs irrespective of the composition of the IAS, as well as by the fact that we occasionally found similar dumbbells in GUV samples produced by cDICE or gel-assisted swelling (Fig. S9 *C* and *D*).

Based on the strong agreement between the model predictions and experimental data, we now inverted the work flow and used the model to calculate the ratio between the line tension σ and osmotic pressure difference $P = P_{ex} - P_{in}$ between the outside and the inside of the vesicle for the measured GUV dumbbell shapes. This ratio can be

calculated directly from the neck radius R_n and opening angles θ_1, θ_2 (Eq. S7 in the supporting material):

$$\frac{\sigma}{P} = \frac{1}{2}R_n^2(\cot\theta_1 + \cot\theta_2). \quad (1)$$

We calculated this ratio for $N = 80$ dumbbell GUVs (Fig. S3) and found a mean value of $-21\ \mu m^2$, which is around half of the measured value for a vesicle that undergoes budding due to phase separation of the membrane into different domains (71).

Arp2/3-nucleated actin networks preferentially assemble at dumbbell necks

Having established that dumbbell GUVs form by a mechanism that is independent of the presence of an actin cortex, we considered them a convenient template on which to study how membrane-nucleated actin cortices react to externally imposed variations in curvature. Due to the low number of dumbbell GUVs produced in one eDICE experiment, we could not directly compare dumbbells from a single experiment with good statistics. The following discussion thus encompasses GUVs from seven different experiments and with several slightly different cortex compositions. We mainly used the human Arp2/3 isoform ArpC1B/C5L, but we obtain similar data for human ArpC1A/C5 and for bovine brain Arp2/3 (Fig. S10 *A*).

We found four different cortical actin distribution phenotypes in dumbbell-shaped GUVs. First, actin could form a continuous and uniform cortex (Fig. 5 *A*). Second, we found GUVs where actin was enriched in a single patch at the GUV neck (Fig. 5 *B*). Third, actin formed a cortex throughout but was enriched in several distinct patches along the neck (Fig. 5 *C*). Fourth, the entire neck could be enriched in actin compared with the rest of the cortex (Fig. 5 *D*). These four phenotypes occurred at roughly the same frequency (around 25% of N = 27 dumbbells; Fig. 5 *E*). Importantly, we found that in cases where actin formed patches, there were always patches present at the neck.

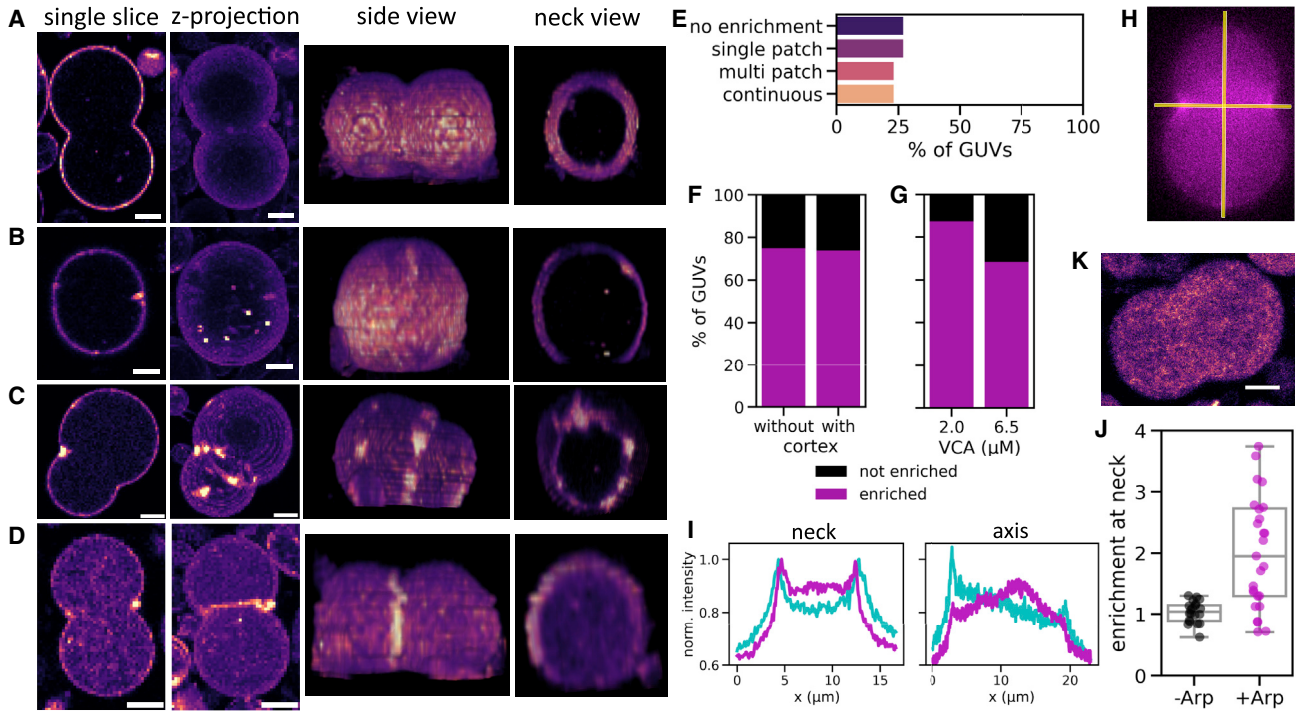

FIGURE 5 Cortical actin networks preferentially localize to dumbbell necks, indicating curvature recognition. (*A–D*) Dumbbell GUVs containing cortical actin showed four phenotypes: actin was evenly distributed (*A*), enriched in a single patch at the neck (*B*), enriched in several distinct patches around the neck (*C*), or enriched in the entire neck region (*D*). Columns show a single confocal slice, a maximum intensity projection, a side view of the 3D-reconstructed z stack, and a view through the neck section in the z stack. Actin intensity is shown in false color (magma) for clarity. (*E*) Bar plot of actin enrichment patterns in dumbbell-shaped GUVs, showing an even distribution over the four groups (A–D) (N = 27 dumbbell GUVs). (*F*) Bar plot shows that 75% of dumbbell-shaped GUVs show actin enrichment at the neck, both for GUVs with and without a continuous actin cortex (N = 23 and 4, respectively). (*G*) Bar plot shows that actin enrichment at the neck was slightly more common in GUVs with 2 μM VCA compared with 6.5 μM VCA (N = 8 and 19, respectively). (*H*) We quantified the amount of actin enrichment at the neck by comparing line intensity profiles across the neck versus the dumbbell's symmetry axis (*yellow lines*). (*I*) Line profiles of membrane (*cyan*) and actin (*magenta*) intensity along the neck and symmetry axis of the dumbbell GUV shown in (*H*), normalized to the maximum pixel value in the neck profiles. Peaks in actin and membrane intensity coincide at the neck, but not at the poles. (*J*) Boxplot of the degree of actin enrichment at dumbbell necks in GUVs where actin nucleated spontaneously in the GUV lumen (−Arp, *black dots*, N = 21) or at the membrane with the help of Arp2/3 (+Arp, *magenta dots*, N = 27). (*K*) Confocal image of a dumbbell where actin polymerized spontaneously in the GUV lumen and does not localize to the neck region. Scale bars, 5 μm.

Rarely, we found a GUV which had bright actin patches both at the neck and elsewhere (Fig. 5 *C*). Preferential actin localization to the neck did not appear to be dependent on the presence of a continuous cortex: we found a few dumbbell GUVs where the cortical region was not significantly enriched in actin compared with the GUV lumen, but also, for these, around 75% exhibited actin enrichment at the neck (Fig. 5 *F*, N = 27 in total). The likelihood that actin was enriched at a dumbbell neck appeared to depend on VCA concentration, with 88% of dumbbells showing neck enrichment at 2 μM VCA, compared with 68% in dumbbells at 6.5 μM VCA (Fig. 5 *G*, N = 8 and 19 GUVs, respectively). This is consistent with our observation that intermediate VCA concentrations were most likely to give rise to deformed patches in spherical GUVs.

We quantified the degree of actin enrichment at the neck by comparing the maximum actin intensity in a line profile through the neck with that measured in a line profile through the dumbbell's axis of rotational symmetry (i.e., along the yellow lines in Fig. 5 *H*, resulting line profiles in Fig. 5 *I*). The degree of actin enrichment in the neck was quite widely spread, ranging from no enrichment ($I_{max,neck}/I_{max,axis} \approx 1$) to an almost fourfold enrichment at the neck compared with the poles ($I_{max,neck}/I_{max,axis} \approx 4$), with a mean enrichment of $I_{max,neck}/I_{max,axis} = 2.2$ (Fig. 5 *J*, magenta points, N = 27).

Importantly, in absence of actin, VCA itself did not preferentially accumulate at dumbbell necks (Fig. S10 *B*). Also, neck enrichment was only present in GUVs where actin was nucleated on the membrane with the help of Arp2/3 and VCA. In GUVs where actin spontaneously nucleated in the GUV lumen without these nucleating proteins, we observed no enrichment at the neck (Fig. 5 *K* and black points (N = 21) in Fig. 5 *J*).

DISCUSSION

To study the interplay of branched actin networks with lipid membranes, we developed a protocol that allows the reproducible and high-yield formation of GUVs with an actin cortex nucleated on the inner surface of the lipid bilayer membrane. Our method is facile, requires small sample volumes, and is fast enough to prevent premature actin polymerization during encapsulation. It is furthermore compatible with a range of widely used lipid compositions (Fig. S13) and different types and concentrations of density gradient media (Fig. S14 *A*). We note that commonly used density gradient media such as Optiprep and sucrose influence actin polymerization kinetics (Fig. S14 *B–E*), highlighting the need for careful experimental design and reporting when encapsulating cytoskeletal polymers.

The new method allowed us to systematically study the formation of actin cortices in GUVs as a function of the concentration of actin and the density of membrane-bound nucleators. We found that Arp2/3-nucleated cortices can grow in different regimes, depending on the amount of actin that is available in the GUV. This allows us to reconcile previous works, which reported that actin forms disconnected patches at low concentrations (3 μM (22)) but continuous actin shells at high concentrations (6.5 μM (27)). This is consistent with the known autocatalytic nucleation mechanism of actin by Arp2/3, which should produce isolated patches: New actin filaments will preferentially be assembled where Arp2/3 can be activated by nucleation promoting factors (73), i.e., at the membrane, and where an existing actin filament is available to act as a primer (8), i.e., in an existing patch. At low density or short filament length (promoted by CP), multiple primers generate independent networks. With increasing actin density and/or filament length, these independent networks can merge into a continuous cortex made of entangled filaments. Irrespective of the actin and VCA concentrations, we found variable phenotypes among GUVs, likely due to a significant variability in protein encapsulation efficiency, which we demonstrated directly by quantitative microscopy. We note that, to form minimal actin cortices, the presence of additional regulatory proteins used in earlier works (profilin, gelsolin, ADF/cofilin, and CP (22, 27)) was not required.

In GUV samples prepared by eDICE, we always observed some dumbbell-shaped GUVs where actin preferentially localized to the neck. These dumbbell GUVs form by a mechanism involving the hemifusion of two nested GUVs, whose combined shape is determined by an interplay of osmotic pressure across the membrane, and line tension in the hemifusion stalk. The observation of preferential localization at the neck suggests that minimal branched actin networks can recognize micrometer-scale membrane curvature. We note that our data do not allow us to distinguish whether actin polymerizes on the membrane and subsequently accumulates at dumbbell necks by lateral diffusion, or whether net actin assembly is favored where the membrane is bent. This distinction would shed light on the mechanism of curvature sensing and generation in branched actin networks and should be followed up on in future works.

Intriguingly, minimal actin networks have been shown to associate with bent membrane patches (22), and our results corroborate this finding (Figs. 2 *F*, S11, and S12). This suggests that actin networks may be able to both sense and generate membrane curvature. Quantitative analysis of actin enrichment as a function of membrane curvature did not reveal any clear correlations (Fig. S11 *D* and *E*). We note, however, that subtle preferences for a specific membrane curvature may easily be obscured by the complex 3D geometry of the dumbbell neck, polydispersity in GUV membrane tension and excess membrane area, and widely varying protein encapsulation efficiencies. Broadly, we find that branched actin networks accumulate where the membrane is inwardly curved in at least one principal direction.

In future studies, the curvature sensitivity of actin should therefore be more systematically studied to gain insight into

its mechanistic origins. In the cell-like environment of a GUV, micropipette aspiration (74) or microfluidic deformation (75) may be used to impose curvature on GUVs with an existing cortex. However, variations in protein encapsulation efficiency will likely complicate the interpretation of such assays. Experiments with non-confining curved membrane geometries would therefore provide a useful alternative. 3D-structured supported lipid bilayers (76) may, for instance, serve as substrates with tunable geometry, on which actin assembly could be observed live and on a variety of membrane geometries.

What exactly mediates network-level curvature sensing remains elusive. It has been suggested that the competition of Arp2/3 and CP for actin monomers may be a driving factor behind the growth of curved actin networks (22), although it remains unclear how this mechanism would lead to membrane curvature generation. We found that CP was not strictly required for the formation of deformed actin patches in spherical GUVs, nor for preferential accumulation of actin at the neck of dumbbell-shaped GUVs. On a molecular scale, the Arp2/3 complex itself has been shown to preferentially bind to actin filaments on their convex side; i.e., binding sites from which the mother filament bends away are preferred (77). This effect has been suggested to be amplified on the network level (77), which may help cells orient polymerization forces effectively in organelles such as the lamellipodium. Curiously, if preferential assembly of actin on convex mother filaments occurs on an inwardly bent piece of membrane, we should expect curvature preference of Arp2/3 to drive nucleation of the densest networks at the sides of the bent membrane patch, rather than in its middle. If we imagine an initially flat membrane decorated with a branched cortex, where all the filament ends are anchored firmly on the membrane, local inward bending should splay apart the actin branches at the sides of this deformation (thus increasing nucleation there), whereas branches would be unaffected or slightly compressed at the tip of the deformation, hence lowering the nucleation rate there. By contrast, we observed that actin intensity peaked at the center of the concave membrane patches, which suggests that a different mechanism is behind the formation of concave membrane patches.

Membrane curvature sensing of actin networks in the absence of curvature-sensitive proteins to mediate actin-membrane interactions has so far, to the best of our knowledge, never been observed. We speculate that it may present a mechanism by which actin assembly can be robustly directed to actin-rich membrane structures with a micrometer-scale curvature, such as the early cytokinetic furrow (78), phagocytic cups (12), or during cell migration. Actin enrichment at curved membrane sites has, for instance, been reported around the nucleus of immune cells squeezing through micrometric constrictions (14), and in fibroblasts or neutrophils migrating on nanopatterned substrates with structure sizes of a few 100 nm (79, 80). Although other proteins certainly contribute to this organization in live cells, our work raises the question of whether an intrinsic curvature sensitivity of branched actin networks may help in making these associations more robust. Similarly, the curvature sensitivity of branched actin networks may potentially be used as a design strategy for building synthetic cells with an actin-based division machinery. Researchers in the growing field of bottom-up synthetic biology are pursuing different strategies to promote membrane constriction based on imposing membrane curvature by microfluidic trapping (75,81) or addition of membrane-shaping proteins (82). Our findings suggest that preferential assembly of actin cortices can be promoted in simpler systems, requiring fewer proteins and thus less careful tuning of encapsulation stoichiometries or *in vesiculo* transcription and translation.

CONCLUSIONS

We developed a robust protocol for actin encapsulation in cell-like lipid containers. We used these actin-containing membrane vesicles to show that branched actin networks are able to recognize membrane curvature, although how this works remains an open question. We observed that cortical actin networks preferentially assembled at the necks of dumbbell-shaped GUVs and were able to form concave membrane patches in spherical GUVs. This finding raises the intriguing possibility that intrinsic curvature sensitivity of branched actin nucleation may contribute to the localization of actin at curved membrane regions in cells such as the early cytokinetic furrow.

CODE AVAILABILITY

A python script to generate the predicted dumbbell shapes from our model, as well as Jupyter notebooks to analyze the experimental data, are available on GitHub: https://github.com/BioSoftMatterGroup/actin-curvature-sensing.

SUPPORTING MATERIAL

Supporting material can be found online at https://doi.org/10.1016/j.bpj.2023.02.018.

AUTHOR CONTRIBUTIONS

All authors contributed to the research design. L.B. and M.A.P. performed all the experiments and analyzed the data. F.F. performed all the theoretical modeling. L.B. wrote the manuscript together with F.F. All authors reviewed, approved, and contributed to the final version of the manuscript.

ACKNOWLEDGMENTS

We thank Jeffrey den Haan for protein purification, Kristina Ganzinger (AMOLF) for providing the 10xHis VCA construct, David Kovar (University of Chicago) for the CP constructs, and Michael Way (Crick Institute) for providing purified human Arp2/3 proteins. We are grateful to Iris Lambert for early actin encapsulation experiments that formed the basis for establishing the eDICE method, to Federico Fanalista for acquiring images of dumbbell-shaped GUVs in samples produced by cDICE, and to

Tom Aarts for images of dumbbell-shaped GUVs produced by gel-assisted swelling. Lennard van Buren is thanked for his help with image analysis to quantify actin concentrations in GUVs. We thank Kristina Ganzinger (AMOLF) for hosting us to perform pyrene assays in her lab, and Balász Antalicz (AMOLF) for technical assistance with the spectrophotometer. The authors also thank Matthieu Piel and Daniel Fletcher for insightful and inspiring discussions. We acknowledge financial support from The Netherlands Organization of Scientific Research (NWO/OCW) Gravitation program Building a Synthetic Cell (BaSyC) (024.003.019). F.F. gratefully acknowledges funding from the Kavli Synergy program of the Kavli Institute of Nanoscience Delft.

SUPPORTING CITATIONS

References (56, 66, 69–72, 83–86) appear in the supporting material.

REFERENCES

1. Chugh, P., and E. K. Paluch. 2018. The actin cortex at a glance. *J. Cell Sci.* 131:jcs186254.
2. Bovellan, M., Y. Romeo, …, G. Charras. 2014. Cellular control of cortical actin nucleation. *Curr. Biol.* 24:1628–1635.
3. Fritzsche, M., R. Thorogate, and G. Charras. 2014. Quantitative analysis of ezrin turnover dynamics in the actin cortex. *Biophys. J.* 106:343–353.
4. Romero, S., C. Le Clainche, …, M. F. Carlier. 2004. Formin is a processive motor that requires profilin to accelerate actin assembly and associated ATP hydrolysis. *Cell.* 119:419–429.
5. Chesarone, M. A., A. G. Dupage, and B. L. Goode. 2010. Unleashing formins to remodel the actin and microtubule cytoskeletons. *Nat. Rev. Mol. Cell Biol.* 11:62–74.
6. Mullins, R. D., J. F. Kelleher, …, T. D. Pollard. 1998. Arp2/3 complex from Acanthamoeba binds profilin and cross-links actin filaments. *Mol. Biol. Cell.* 9:841–852.
7. Blanchoin, L., K. J. Amann, …, T. D. Pollard. 2000. Direct observation of dendritic actin filament networks nucleated by Arp2/3 complex and WASP/Scar proteins. *Nature.* 404:1007–1011.
8. Achard, V., J. L. Martiel, …, R. Boujemaa-Paterski. 2010. A "primer"--based mechanism underlies branched actin filament network formation and motility. *Curr. Biol.* 20:423–428.
9. Arnold, J. M. 1969. Cleavage furrow formation in a telolecithal egg (loligo pealii): I. Filaments in Early Furrow Formation. *J. Cell Biol.* 41:894–904.
10. Schroeder, T. E. 1968. Preliminary notes. Cytokinesis: filaments in the cleavage furrow. *Exp. Cell Res.* 53:272–276.
11. Fedorov, E. G., and T. Shemesh. 2017. Physical model for stabilization and repair of trans-endothelial apertures. *Biophys. J.* 112:388–397.
12. Clarke, M., U. Engel, …, G. Gerisch. 2010. Curvature recognition and force generation in phagocytosis. *BMC Biol.* 8:154.
13. Chen, T., A. Callan-Jones, …, B. Ladoux. 2019. Large-scale curvature sensing by directional actin flow drives cellular migration mode switching. *Nat. Phys.* 15:393–402.
14. Thiam, H. R., P. Vargas, …, M. Piel. 2016. Perinuclear Arp2/3-driven actin polymerization enables nuclear deformation to facilitate cell migration through complex environments. *Nat. Commun.* 7:10997.
15. Peter, B. J., H. M. Kent, …, H. T. McMahon. 2004. BAR domains as sensors of membrane curvature: the amphiphysin BAR structure. *Science.* 303:495–499.
16. Tsujita, K., S. Suetsugu, …, T. Takenawa. 2006. Coordination between the actin cytoskeleton and membrane deformation by a novel membrane tubulation domain of PCH proteins is involved in endocytosis. *J. Cell Biol.* 172:269–279.
17. Carman, P. J., and R. Dominguez. 2018. BAR domain proteins—a linkage between cellular membranes, signaling pathways, and the actin cytoskeleton. *Biophys. Rev.* 10:1587–1604.
18. Tsai, F. C., A. Bertin, …, P. Bassereau. 2018. Ezrin enrichment on curved membranes requires a specific conformation or interaction with a curvature-sensitive partner. *Elife.* 7:e37262.
19. Bridges, A. A., M. S. Jentzsch, …, A. S. Gladfelter. 2016. Micron-scale plasma membrane curvature is recognized by the septin cytoskeleton. *J. Cell Biol.* 213:23–32.
20. Mavrakis, M., Y. Azou-Gros, …, T. Lecuit. 2014. Septins promote F-actin ring formation by crosslinking actin filaments into curved bundles. *Nat. Cell Biol.* 16:322–334.
21. Palani, S., S. Ghosh, …, D. V. Köster. 2021. Calponin-homology domain mediated bending of membrane-associated actin filaments. *Elife.* 10:e61078.
22. Dürre, K., F. C. Keber, …, A. R. Bausch. 2018. Capping protein-controlled actin polymerization shapes lipid membranes. *Nat. Commun.* 9:1630.
23. Simon, C., R. Kusters, …, C. Sykes. 2019. Actin dynamics drive cell-like membrane deformation. *Nat. Phys.* 15:602–609.
24. Fischer-Friedrich, E., Y. Toyoda, …, F. Jülicher. 2016. Rheology of the active cell cortex in mitosis. *Biophys. J.* 111:589–600.
25. Fläschner, G., C. I. Roman, …, D. J. Müller. 2021. Rheology of rounded mammalian cells over continuous high-frequencies. *Nat. Commun.* 12:2922.
26. Murrell, M., L. L. Pontani, …, C. Sykes. 2011. Spreading dynamics of biomimetic actin cortices. *Biophys. J.* 100:1400–1409.
27. Pontani, L. L., J. van der Gucht, …, C. Sykes. 2009. Reconstitution of an actin cortex inside a liposome. *Biophys. J.* 96:192–198.
28. Carvalho, K., F. C. Tsai, …, C. Sykes. 2013. Cell-sized liposomes reveal how actomyosin cortical tension drives shape change. *Proc. Natl. Acad. Sci. USA.* 110:16456–16461.
29. Tsai, F.-C., and G. H. Koenderink. 2015. Shape control of lipid bilayer membranes by confined actin bundles. *Soft Matter.* 11:8834–8847.
30. Litschel, T., C. F. Kelley, …, P. Schwille. 2021. Reconstitution of contractile actomyosin rings in vesicles. *Nat. Commun.* 12:2254.
31. Bashirzadeh, Y., S. A. Redford, …, A. P. Liu. 2021. Actin crosslinker competition and sorting drive emergent GUV size-dependent actin network architecture. *Commun. Biol.* 4:1136.
32. Loiseau, E., J. A. M. Schneider, …, A. R. Bausch. 2016. Shape remodeling and blebbing of active cytoskeletal vesicles. *Sci. Adv.* 2:e1500465.
33. Maan, R., E. Loiseau, and A. R. Bausch. 2018. Adhesion of active cytoskeletal vesicles. *Biophys. J.* 115:2395–2402.
34. Reeves, J. P., and R. M. Dowben. 1969. Formation and properties of thin-walled phospholipid vesicles. *J. Cell. Physiol.* 73:49–60.
35. Walde, P., K. Cosentino, …, P. Stano. 2010. Giant vesicles: preparations and applications. *Chembiochem.* 11:848–865.
36. Horger, K. S., D. J. Estes, …, M. Mayer. 2009. Films of agarose enable rapid formation of giant liposomes in solutions of physiologic ionic strength. *J. Am. Chem. Soc.* 131:1810–1819.
37. López Mora, N., J. S. Hansen, …, A. Kros. 2014. Preparation of size tunable giant vesicles from cross-linked dextran(ethylene glycol) hydrogels. *Chem. Commun.* 50:1953–1955.
38. Pazzi, J., M. Xu, and A. B. Subramaniam. 2019. Size distributions and yields of giant vesicles assembled on cellulose papers and cotton fabric. *Langmuir.* 35:7798–7804.
39. Angelova, M. I., and D. S. Dimitrov. 1986. Liposome electroformation. *Faraday Discuss. Chem. Soc.* 81:303–311.
40. Montes, L. R., A. Alonso, …, L. A. Bagatolli. 2007. Giant unilamellar vesicles electroformed from native membranes and organic lipid mixtures under physiological conditions. *Biophys. J.* 93:3548–3554.
41. Pott, T., H. Bouvrais, and P. Méléard. 2008. Giant unilamellar vesicle formation under physiologically relevant conditions. *Chem. Phys. Lipids.* 154:115–119.

42. Weiss, M., J. P. Frohnmayer, …, J. P. Spatz. 2018. Sequential bottom-up assembly of mechanically stabilized synthetic cells by microfluidics. *Nat. Mater.* 17:89–96.

43. Abate, A. R., T. Hung, …, D. A. Weitz. 2010. High-throughput injection with microfluidics using picoinjectors using picoinjectors. *Proc. Natl. Acad. Sci. USA.* 107:19163–19166.

44. Pautot, S., B. J. Frisken, and D. A. Weitz. 2003. Production of unilamellar vesicles using an inverted emulsion. *Langmuir.* 19:2870–2879.

45. Deshpande, S., and C. Dekker. 2018. On-chip microfluidic production of cell-sized liposomes. *Nat. Protoc.* 13:856–874.

46. Yandrapalli, N., J. Petit, …, T. Robinson. 2021. Surfactant-free production of biomimetic giant unilamellar vesicles using PDMS-based microfluidics. *Commun. Chem.* 4:100.

47. Tivony, R., M. Fletcher, …, U. F. Keyser. 2021. A microfluidic platform for sequential assembly and separation of synthetic cell models. *ACS Synth. Biol.* 10:3105–3116.

48. Deng, N. N., M. Yelleswarapu, and W. T. S. Huck. 2016. Monodisperse uni- and multicompartment liposomes. *J. Am. Chem. Soc.* 138:7584–7591.

49. Abkarian, M., E. Loiseau, and G. Massiera. 2011. Continuous droplet interface crossing encapsulation (cDICE) for high throughput monodisperse vesicle design. *Soft Matter.* 7:4610–4614.

50. Claudet, C., M. In, and G. Massiera. 2016. Method to disperse lipids as aggregates in oil for bilayers production. *Eur. Phys. J. E Soft Matter.* 39:9.

51. Göpfrich, K., B. Haller, …, J. P. Spatz. 2019. One-pot assembly of complex giant unilamellar vesicle-based synthetic cells. *ACS Synth. Biol.* 8:937–947.

52. Moga, A., N. Yandrapalli, …, T. Robinson. 2019. Optimization of the inverted emulsion method for high-yield production of biomimetic giant unilamellar vesicles. *Chembiochem.* 20:2674–2682.

53. Bashirzadeh, Y., N. Wubshet, …, A. P. Liu. 2021. Rapid encapsulation of reconstituted cytoskeleton inside giant unilamellar vesicles. *J. Vis. Exp.* 177:e63332.

54. Luo, T., V. Srivastava, …, D. N. Robinson. 2014. Mimicking the mechanical properties of the cell cortex by the self-assembly of an actin cortex in vesicles. *Appl. Phys. Lett.* 104:153701.

55. Deek, J., R. Maan, …, A. R. Bausch. 2018. Reconstitution of composite actin and keratin networks in vesicles. *Soft Matter.* 14:1897–1902.

56. Van de Cauter, L., F. Fanalista, …, K. A. Ganzinger. 2021. Optimized cDICE for efficient reconstitution of biological systems in giant unilamellar vesicles. *ACS Synth. Biol.* 10:1690–1702.

57. Shekhar, S., and M. F. Carlier. 2017. Enhanced depolymerization of actin filaments by ADF/cofilin and monomer funneling by capping protein cooperate to accelerate barbed-end growth. *Curr. Biol.* 27:1990–1998.e5.

58. Alvarado, J., and G. H. Koenderink. 2015. Reconstituting cytoskeletal contraction events with biomimetic actin-myosin active gels. *In* Building a Cell from its Component Parts. Methods in Cell Biology, *volume 128*. J. Ross and W. F. Marshall, eds Academic Press, pp. 83–103.

59. Sonal, K. A. Ganzinger, …, P. Schwille. 2019. Myosin-II activity generates a dynamic steady state with continuous actin turnover in a minimal actin cortex. *J. Cell Sci.* 132:jcs299899.

60. Baldauf, L., F. Frey, …, G. H. Koenderink. 2023. Biomimetic actin cortices shape cell-sized lipid vesicles. Preprint at bioRxiv. https://doi.org/10.1101/2023.01.15.524117.

61. Burke, T. A., A. J. Harker, …, D. R. Kovar. 2017. The bacterial virulence factors VopL and VopF nucleate actin from the pointed end. *J. Cell Biol.* 216:1267–1276.

62. Xu, J., W. H. Schwarz, …, T. D. Pollard. 1998. Mechanical properties of actin filament networks depend on preparation, polymerization conditions, and storage of actin monomers. *Biophys. J.* 74:2731–2740.

63. Aitken, C. E., R. A. Marshall, and J. D. Puglisi. 2008. An oxygen scavenging system for improvement of dye stability in single-molecule fluorescence experiments. *Biophys. J.* 94:1826–1835.

64. Claessens, M. M. A. E., F. A. M. Leermakers, …, M. A. C. Stuart. 2008. Osmotic shrinkage and reswelling of giant vesicles composed of dioleoylphosphatidylglycerol and cholesterol. *Biochim. Biophys. Acta.* 1778:890–895.

65. Schindelin, J., I. Arganda-Carreras, …, A. Cardona. 2012. Fiji: an open-source platform for biological-image analysis. *Nat. Methods.* 9:676–682.

66. van Buren, L., G. H. Koenderink, and C. Martinez-Torres. 2023. DisGUVery: a versatile open-source software for high-throughput image analysis of giant unilamellar vesicles. *ACS Synth. Biol.* 12:120–135.

67. Mary, H., and G. J. Brouhard. 2019. Kappa (κ): analysis of curvature in biological image data using B-splines. Preprint at bioRxiv. https://doi.org/10.1101/852772.

68. Egile, C., T. P. Loisel, …, M. F. Carlier. 1999. Protein promotes actin nucleation by Arp2/3 complex and bacterial actin-based motility. *J. Cell Biol.* 146:1319–1332.

69. Jülicher, F., and R. Lipowsky. 1993. Domain-induced budding of vesicles. *Phys. Rev. Lett.* 70:2964–2967.

70. Jülicher, F., and R. Lipowsky. 1996. Shape transformations of vesicles with intramembrane domains. *Phys. Rev. E.* 53:2670–2683.

71. Baumgart, T., S. T. Hess, and W. W. Webb. 2003. Imaging coexisting fluid domains in biomembrane models coupling curvature and line tension. *Nature.* 425:821–824.

72. Allain, J. M., and M. Ben Amar. 2006. Budding and fission of a multiphase vesicle. *Eur. Phys. J. E Soft Matter.* 20:409–420.

73. Yamaguchi, H., H. Miki, …, T. Takenawa. 2000. Two tandem verprolin homology domains are necessary for a strong activation of Arp2/3 complex-induced actin polymerization and induction of microspike formation by N-WASP. *Proc. Natl. Acad. Sci. USA.* 97:12631–12636.

74. Guevorkian, K., and J. L. Maître. 2017. Micropipette aspiration: a unique tool for exploring cell and tissue mechanics in vivo. *In* Cell Polarity and Morphogenesis. Methods in Cell Biology, *volume 139*. T. Lecuit, ed Academic Press, pp. 187–201.

75. Ganzinger, K. A., A. Merino-Salomón, …, P. Schwille. 2020. FtsZ reorganization facilitates deformation of giant vesicles in microfluidic traps. *Angew. Chem. Int. Ed. Engl.* 59:21372–21376.

76. Rinaldin, M., P. Fonda, …, D. J. Kraft. 2020. Geometric pinning and antimixing in scaffolded lipid vesicles. *Nat. Commun.* 11:4314.

77. Risca, V. I., E. B. Wang, …, D. A. Fletcher. 2012. Actin filament curvature biases branching direction. *Proc. Natl. Acad. Sci. USA.* 109:2913–2918.

78. Chan, F. Y., A. M. Silva, …, A. X. Carvalho. 2019. The ARP2/3 complex prevents excessive formin activity during cytokinesis. *Mol. Biol. Cell.* 30:96–107.

79. Galic, M., S. Jeong, …, T. Meyer. 2012. External push and internal pull forces recruit curvature-sensing N-BAR domain proteins to the plasma membrane. *Nat. Cell Biol.* 14:874–881.

80. Brunetti, R. M., G. Kockelkoren, …, O. D. Weiner. 2022. WASP integrates substrate topology and cell polarity to guide neutrophil migration. *J. Cell Biol.* 221:e202104046.

81. Fanalista, F., A. Birnie, …, C. Dekker. 2019. Shape and size control of artificial cells for bottom-up biology. *ACS Nano.* 13:5439–5450.

82. Steinkühler, J., R. L. Knorr, …, R. Lipowsky. 2020. Controlled division of cell-sized vesicles by low densities of membrane-bound proteins. *Nat. Commun.* 11:905.

83. Baumgart, T., S. Das, …, J. T. Jenkins. 2005. Membrane elasticity in giant vesicles with fluid phase coexistence. *Biophys. J.* 89:1067–1080.

84. Weinberger, A., F. C. Tsai, …, C. Marques. 2013. Gel-assisted formation of giant unilamellar vesicles. *Biophys. J.* 105:154–164.

85. Cooper, J. A., S. B. Walker, and T. D. Pollard. 1983. Pyrene actin: documentation of the validity of a sensitive assay for actin polymerization. *J. Muscle Res. Cell Motil.* 4:253–262.

86. Doolittle, L. K., M. K. Rosen, and S. B. Padrick. 2013. Measurement and analysis of in vitro actin polymerization. *In* Adhesion Protein Protocols. A. S. Coutts, ed Humana Press, pp. 273–293.

Biophysical Journal, Volume *122*

Supplemental information

Branched actin cortices reconstituted in vesicles sense membrane curvature

Lucia Baldauf, Felix Frey, Marcos Arribas Perez, Timon Idema, and Gijsje H. Koenderink

Supporting Material:
Branched actin cortices reconstituted in vesicles sense membrane curvature

Lucia Baldauf[1,2,*], Felix Frey[1,3,*], Marcos Arribas Perez[1], Timon Idema[1,†], and Gijsje H. Koenderink[1,**]

[1] Department of Bionanoscience, Kavli Institute of Nanoscience Delft, Delft University of Technology, Van der Maasweg 9, 2629 HZ Delft, The Netherlands
[2] Present address: London Centre for Nanotechnology, University College London, London WCH1 0AW, UK
[3] Present address: Institute of Science and Technology Austria, 3400 Klosterneuburg, Austria
[*] These authors contributed equally to this work.
[†] Correspondence: t.idema@tudelft.nl
[**] Correspondence: g.h.koenderink@tudelft.nl

I. THEORETICAL MODEL OF EQUILIBRIUM SHAPES OF DUMBBELL VESICLES

As described in the main text, we assume that a dumbbell GUV is created of two vesicles, a larger outer one containing a smaller inner one, of which the inner one has burst, resulting in a shape with two lobes: one with a single and the other with a double membrane bilayer (Fig. S1). Here we study the shape of these dumbbells. Our approach is motivated by earlier theoretical work on domain-induced budding of vesicles composed of phase-separating lipid mixtures [1–4]. First we explain why the dumbbell shape can be described by two spherical caps, and second we explain how we infer the ratio between line tension and vesicle pressure from the shape of the GUV.

The shape energy of a GUV with negligible bending energy is given by [2]:

$$\mathcal{H} = \oint_{\partial 1} \sigma \, \mathrm{d}l + \Sigma^{(1)} A^{(1)} + \Sigma^{(2)} A^{(2)} + PV \, . \tag{S1}$$

The first term in Eq. (S1) describes the energy associated with the perimeter of the interface between the double bilayer surface and the single bilayer surface. Therefore, the integral runs along the edge of this interface, where σ is the line tension. The second and the third term correspond to the membrane tension, where A_i is the surface area and $\Sigma^{(i)}$ is the membrane tension of domain i, with $i = 1$ for the double membrane and $i = 2$ for the single membrane domain. The fourth term introduces a volume constraint, where P is the pressure difference $P = P_{\mathrm{ex}} - P_{\mathrm{in}}$ between the outside and the inside of the GUV and V is the volume of the GUV.

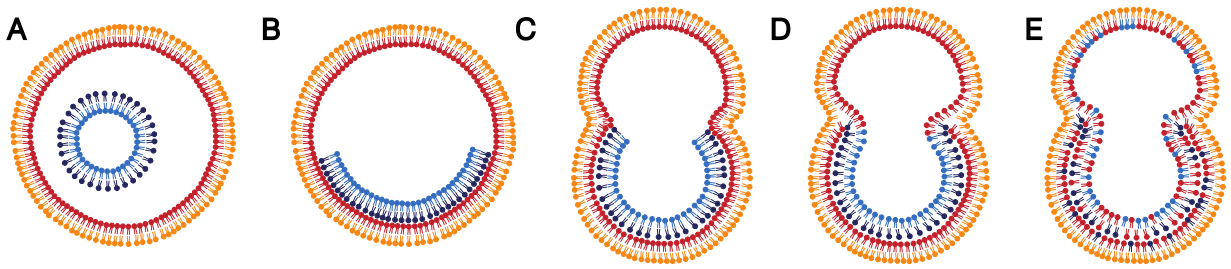

FIG. S1. **Schematic of dumbbell vesicle formation from nested GUVs.** (A) During GUV formation, nested vesicles are created. The leaflets of the outer GUV are shown in orange (outer) and red (inner) and the leaflets of the inner GUV are shown in black (outer) and blue (inner). (B) After the inner vesicle bursts, it leaks its entire volume into the GUV. (C) The membrane of the inner vesicle merges along its edge with the outer GUV. (D) The membranes of the inner vesicle and the outer GUV undergo hemifusion. (E) The lipids within the same membrane leaflet mix. At the interface, where the double bilayer and single bilayer meet, a line tension emerges that leads to the formation of a dumbbell vesicle.

We consider the limiting case where the energy associated with the line tension and the volume constraint dominate the system, and thus the contribution of the bending energy is negligible in Eq. (S1). This assumption can be justified by estimating the various energy contributions based on typical parameter values. For simplicity, we consider a sphere with radius $10\,\mu$m, which is the limiting case of a dumbbell with equal cap sizes and maximum opening angles. We assume a pressure difference of $P \sim 0.02\,\mathrm{Nm}^{-2}$ [3], a membrane tension of $\Sigma \sim 10^{-7}\,\mathrm{Nm}^{-1}$ [3] (neglecting differences between the two half spheres), a line tension of $\sigma \sim 1\,\mathrm{pN}$ [3] and a bending rigidity of $\kappa \sim 10^2\,\mathrm{pN\,nm}$ [3]. Using

Eq. (S1) and the bending energy of two half spheres, one with a double bilayer lobe and one with a single bilayer lobe ($8\pi\kappa + 4\pi\kappa$), we get: $E_{\text{pressure}} \sim 80\,\text{nN nm}$, $E_{\text{tension}} \sim 100\,\text{nN nm}$, $E_{\text{line}} \sim 60\,\text{nN nm}$ and $E_{\text{bending}} \sim 4\,\text{nN nm}$. Since the bending energy is over an order of magnitude smaller than the other contributions, we can neglect the energy contribution of membrane bending.

Since dumbbell shapes are axisymmetric, we can parameterize them by a (trivial) rotation angle ϕ about the symmetry axis, and a contour length s along their shape, see Fig. S2. The shape and local orientation of the contour can then be described by the radial position $r(s)$ and the tangent angle $\Psi(s)$. These parameters satisfy the geometric constraint $\dot{r} = \cos\Psi$, with a dot denoting the derivative with respect to the arc length s. To enforce this constraint, we add a term $\gamma(\dot{r} - \cos\Psi)$ to the shape energy, where γ is a Lagrange multiplier. We can then write the shape energy as the integral over an energy density

$$\begin{aligned}\mathcal{H} = \oint_{\partial 1} \sigma \,\mathrm{d}l + 2\pi \int_{s_0}^{s_1} \left[\Sigma^{(1)} r(s) + \frac{1}{2} P r^2 \sin\psi(s) + \gamma\left(\dot{r} - \cos\psi(s)\right)\right] \mathrm{d}s \\ + 2\pi \int_{s_1}^{s_2} \left[\Sigma^{(2)} r(s) + \frac{1}{2} P r^2 \sin\psi(s) + \gamma\left(\dot{r} - \cos\psi(s)\right)\right] \mathrm{d}s. \end{aligned} \tag{S2}$$

We can minimize the energy density within each domain, which gives us the following shape equations [2]:

$$0 = \frac{1}{2} P r^2 \cos\psi + \gamma \sin\psi, \tag{S3a}$$

$$\dot{\gamma} = \Sigma^{(i)} + P r \sin\psi, \tag{S3b}$$

$$\dot{r} = \cos\psi. \tag{S3c}$$

Moverover, we get a matching condition at the boundary ($s = s_1$), where there is a jump in the tangent angle ψ:

$$\lim_{\varepsilon \downarrow 0} \left[\gamma(s_1 + \varepsilon) - \gamma(s_1 - \varepsilon)\right] = \sigma. \tag{S4}$$

The spherical caps can be parametrized by $\psi(s) = s/R_i$ and $r(s) = R_i \sin(s/R_i)$. We solve Eq. (S3a) for γ, using the parametrization of the spherical caps, take the derivative with respect to s and use the resulting expression in Eq. (S3b). As a result, we find an equation for the pressure difference P and the Lagrange multiplier γ.

$$P = -\frac{2\Sigma^{(i)}}{R_i}, \tag{S5}$$

$$\gamma = -\frac{1}{2} P R_i^2 \sin\psi\cos\psi = \Sigma^{(i)} R_i \sin\psi\cos\psi \tag{S6}$$

Hence, if P and γ fulfill Eqs. (S5)-(S6), the dumbbell shape necessarily fulfills Eqs. (S3)-(S4). Therefore, the dumbbell shape is a minimal energy shape (with the boundary condition defined through Eq. (S4)), as previously noted by Baumgart et al. [3] or Allain and Ben Amar [4].

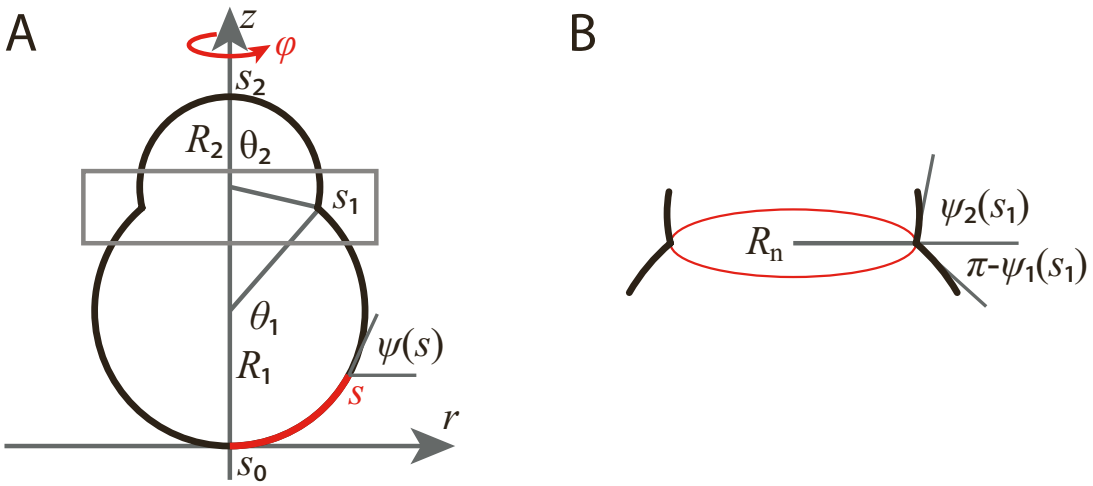

FIG. S2. **Geometry of dumbbell GUVs.** (A) Parametrization of the dumbbell shape by the arc length s (red) along the (rotationally symmetric) membrane contour. We take $s_0 = 0$ at the south pole of the dumbbell. The local orientation of the membrane is given by the angle $\psi(s)$. The bright and dim lobes are spherical caps characterized by their radii R_1 and R_2 and their opening angles at the neck, θ_1 and θ_2. The neck is located at $s = s_1$, and the north pole at $s = s_2$. (B) Zoom-in to the dumbbell neck region (grey rectangle, panel A). The line tension of the hemifusion line (red) determines the neck radius R_n. Dumbbell lobes connect to the plane of the neck at angles $\pi - \psi_1$ and ψ_2, respectively.

Eq. (S5) is the well-known Laplace pressure, relating the pressure difference across the membrane to the membrane's surface tension. Eq. (S6) gives us the value of the Lagrange multiplier γ in each domain. The two domains meet at the neck, where $R_1 \sin\theta_1 = R_2 \sin\theta_2 = R_\mathrm{n}$. Using the expressions for γ in the matching condition, Eq. (S4), with $\psi_1 = \theta_1$ and $\psi_2 = \pi - \theta_2$, allows us to calculate the ratio between the line tension σ and the pressure gradient P [3, 5]:

$$\frac{\sigma}{P} = \frac{1}{2} R_\mathrm{n}^2 \left(\cot\psi_1 - \cot\psi_2\right) = \frac{1}{2} R_\mathrm{n}^2 \left(\cot\theta_1 + \cot\theta_2\right) \tag{S7}$$

Fig. S3 shows the histogram of the ratio σ/P (blue) calculated from the measured GUV dumbbell shapes (cf. main text Fig. 4 G,H), according to Eq. (S7). Here, the opening angles of the bright and dark lobe of the dumbbell GUV, θ_1 and θ_2, are calculated from the diameters of the bright and dim lobe and the neck diameter of the GUV. The mean of the histogram (red) is at $-21\,\mu\mathrm{m}^2$, which is about half of the measured value for a vesicle that undergoes domain-induced budding ($-49\,\mu\mathrm{m}^2$) [3]. We note that the value of the ratio σ/P is negative because the (positive) pressure within the vesicle surmounts the pressure in the environment so that the pressure difference P is negative.

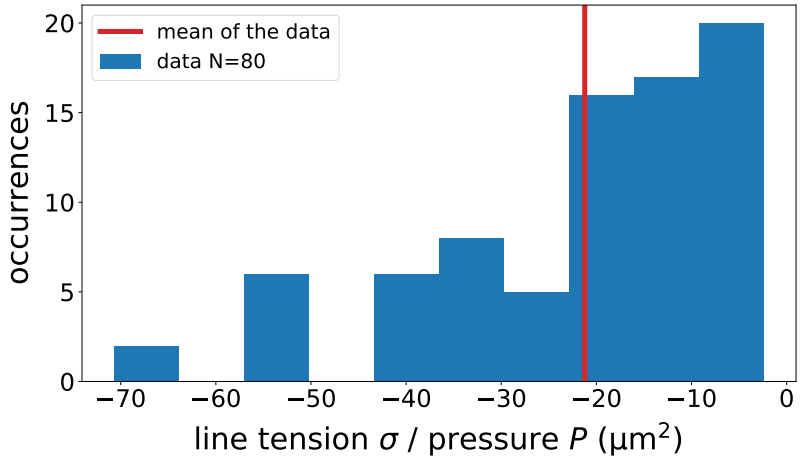

FIG. S3. Histogram of the line tension σ divided by the GUV pressure difference P calculated from the measured GUV dumbbell shapes (main text Fig. 4 G,H), according to Eq. (S7).

II. MODELING THE FORMATION OF DUMBBELL SHAPED GUVS

In the model, the total membrane area (the surface area plus excess membrane area) of the bursting vesicle A_v equals the surface area of the double bilayer membrane lobe A_1, i.e. $A_\mathrm{v} = A_1$. In addition, the GUV's total membrane area A_tot minus the surface area of the bursting lobe A_1 equals the surface area of the single bilayer membrane lobe A_2, i.e., $A_\mathrm{tot} - A_1 = A_2$ (Fig. 4 B of the main text). We calculated the radius of the bright lobe, R_1, from the total membrane area of the bursting vesicle, A_v,

$$R_1(\theta_1, A_\mathrm{v}) = \sqrt{\frac{A_\mathrm{v}}{2\pi(1-\cos\theta_1)}}\,, \tag{S8}$$

where θ_1 is the opening angle of the spherical cap. Similarly, we calculated the radius of the dim lobe, R_2,

$$R_2(\theta_2, A_\mathrm{v}, A_\mathrm{tot}) = \sqrt{\frac{A_\mathrm{tot} - A_\mathrm{v}}{2\pi(1-\cos\theta_2)}}\,, \tag{S9}$$

where θ_2 is the opening angle of the spherical cap. The two caps are connected at a circular interface with neck radius

$$R_\mathrm{n} = R_1 \sin\theta_1 = R_2 \sin\theta_2 \quad \rightarrow \quad R_2 = R_1 \frac{\sin\theta_1}{\sin\theta_2}\,. \tag{S10}$$

By equating Eq. (S9) with Eq. (S10) we obtain

$$\cos\theta_2(\theta_1, A_\mathrm{v}, A_\mathrm{tot}) = \frac{A_\mathrm{v}}{A_\mathrm{tot} - A_\mathrm{v}}\,(1+\cos\theta_1) - 1\,. \tag{S11}$$

The total volume of the GUV is given by adding up the volumes of the spherical caps of the bright and dark lobe

$$V(R_1, R_2, \theta_1, \theta_2) = \frac{\pi}{3} R_1^3\,(2+\cos\theta_1)\,(1-\cos\theta_1)^2 + \frac{\pi}{3} R_2^3\,(2+\cos\theta_2)\,(1-\cos\theta_2)^2\,. \tag{S12}$$

By substituting Eqs. (S8), (S9) and (S11) in Eq. (S12), we got an expression for the volume $V = V(\theta_1, A_\mathrm{tot}, A_\mathrm{v})$ of the GUV that only depends on θ_1, A_tot and A_v.

To connect the shape description derived above to the experiments, we calculated the geometrical correlations between the diameter of the bright and dim lobes from experimental data. First, we assumed that in the model, similar to the experiments, GUVs are created with excess membrane area that allows the GUV to change shape at constant volume. Therefore, the total membrane area A is larger than the surface area $A_\mathrm{s} = 4\pi R^2$, where R is the radius of the spherical GUV. In this case, the reduced area is given by $\nu = A/A_\mathrm{s}$, which varies across GUVs. Next, we sampled two radii $R_\mathrm{tot}, R_\mathrm{v}$ from the measured diameter distribution of GUVs (Fig. 1 C of the main text) that represent the sizes of the outer vesicle and the enclosed vesicle, respectively. From the radii $R_\mathrm{tot}, R_\mathrm{v}$ and the reduced areas $\nu_\mathrm{tot}, \nu_\mathrm{v}$ we calculated the GUV total membrane area,

$$A_\mathrm{tot} = 4\pi R_\mathrm{tot}^2 \nu_\mathrm{tot}\,, \tag{S13}$$

and the total membrane area of the enclosed vesicle,

$$A_\mathrm{v} = 4\pi R_\mathrm{v}^2 \nu_\mathrm{v}\,. \tag{S14}$$

We calculated the initial (spherical) GUV volume $V^* = 4\pi R_\mathrm{tot}^3/3$ and set V^* equal to the dumbbell volume obtained from Eq. (S12),

$$V(\theta_1, A_\mathrm{tot}, A_\mathrm{v}) = V^*\,. \tag{S15}$$

We solved Eq. (S15) for θ_1 by using the values of A_tot and A_v from Eqs. (S13) and (S14). With the value of θ_1 and the values of A_tot and A_v we could calculate the remaining quantities, where we determine θ_2, R_1, R_2 and R_n from Eqs. (S11), (S8), (S9) and (S10), respectively. Together, θ_1, θ_2, R_1, and R_2 define the GUV dumbbell shape.

III. SUPPLEMENTAL EXPERIMENTAL METHODS

A. Supplemental materials

Cholesterol (3β-Hydroxy-5-cholestene, 5-Cholesten-3β-ol, Cat. # C8667-1G) and sucrose (Cat. # S0389) were purchased from Sigma Aldrich. The following lipids were purchased from Avanti Polar Lipids: L-α-phosphatidylcholine (95 %) from chicken egg (EggPC), 1,2-dioleoyl-sn-glycero-3-phospho-L-serine (DOPS), 1,2-dioleoyl-sn-glycero-3-phospho-(1'-myo-inositol-4',5'-bisphosphate) (ammonium salt) (PIP_2), 1',3'-bis[1,2-dioleoyl-sn-glycero-3-phospho]-glycerol (sodium salt) (cardiolipin), and 1,2-dioleoyl-sn-glycero-3-phosphoethanolamine-N-(cap biotinyl) (biotin-PE). PIP_2 was stored in a mixture of chloroform, methanol and water at a 20:9:1 volumetric ratio, all other lipids were stored in chloroform and under argon at -20° C.

B. Supplemental microscopy methods

Widefield microscopy images were acquired on an inverted Leica Thunder Imager widefield microscope equipped with a 200 mW solid state LED5 light source, a 63x water immersion microscope (HC PL APO 63x / 1.20 W Corr CS2) and a monochrome sCMOS camera (Leica). Epifluorescence images were also acquired on an inverted Nikon Ti Eclipse microscope equipped with a 60x water immersion objective (CFI Plan Apochromat VC), a digital CMOS camera (Orca Flash 4.0), and an LED light source (Lumencor Spectra Pad X). Phase contrast images were acquired on the same Nikon Ti microscope using its DIA illuminator at a voltage of 12 V and using the corresponding phase mask in the microscope's condenser.

C. GUV production by gel-assisted swelling

Gel-assisted swelling of GUVs was performed following Ref. [6]. Cover glasses (22 x 22 mm, No. 1.5H, Paul Marienfield GmbH & Co. KG) were first rinsed with ethanol and MilliQ water and dried under a stream of nitrogen. They were then plasma cleaned for 30 seconds (PlasmaPrep III, SPI supplies), after which 100 μL of a solution of 5 % (w/v) polyvinyl alcohol (PVA, 145 kDA, 98 % hydrolysed, VWR, Amsterdam the Netherlands) in 200 mM sucrose in MilliQ water was spread over each coverslip at room temperature. The gel was solidified by baking it in an oven for 30 minutes at 50° C. Then, 10 μL of a lipid solution at a total lipid concentration of 1 mg/mL in chloroform, consisting of DOPC:Atto488-DOPE at a molar ratio of 99.5:0.5, was spread over the gel. The gel was placed in a vacuum desiccator for 30 minutes to ensure total evaporation of the organic solvent. The cover glasses were then placed in a compartmentalized petri dish (4 compartments, VWR), and to each gel we gently added 300 μL of GUV swelling buffer (10 mM Tris-HCl at pH 7.4, 100 mM KCl, 100 mOsm sucrose). After swelling for one hour, GUVs were collected by taking up the swelling solution with a pipette (1 mL tip), flushing the solution again over the cover slip once to dislodge the GUVs, and pipetting it up again.

D. GUV production by cDICE

cDICE GUVs were prepared from the same solutions and in the same rotating chamber as eDICE GUVs. Droplets were formed by injecting IAS into the oil phase at a rate of 25 μL/min for 5 min using a syringe pump (KDS 100 CE, KD Scientific). The capillary setup was identical to that described in [7].

E. Actin polymerization assays

Actin polymerization was quantified by the classical pyrene actin assay [8], following an existing protocol [9], briefly summarized below.

a. Hardware Pyrene assays were performed on a Duetta fluorescence and absorbance spectrometer (Horiba Scientific), equipped with an 80 W S/N 1344-DL lamp and TC1 temperature controller (Quantum Northwest). The temperature varied between 25.0 and 25.4 ° C. Measurements were performed following a custom-defined procedure in the Horiba EzSpec software. For an excitation wavelength of 365 nm, the emission at 407 nm was recorded for a 1 s integration time per data point. The excitation window was set at 10 nm and the emission window at 5 nm. These parameters were chosen to maximise the relative difference in intensity between polymerized and unpolymerized

pyrene-actin samples. All samples were measured in 3-window Quarz microvolume cuvettes from Hellma Analytics with an optical path length of 3 mm, holding 55 μL sample volumes. Cuvettes were cleaned by rinsing with 5 mL MilliQ water, 2 mL ethanol, and 2 mL MilliQ water between measurements, and dried under N_2 stream. Between different days of measurements, the cuvettes were further cleaned by sonicating in a 1 % Hellmanex solution for 5 min, sonicating for 5 min in MilliQ water to remove any excess detergent, and finally rinsing with 5 mL MilliQ water before drying under N_2 stream.

b. Procedure We performed all experiments in a final buffer with the same composition as the GUV IAS buffer, with at least two independent measurements per condition. Measurements with the different Arp2/3 isoforms but no Optiprep in the buffer were performed once per isoform. The final concentrations of actin, VCA and Arp2/3 complex were 4 μM, 650 nM, and 50 nM, respectively. We first prepared an actin premix to ensure a consistent starting concentration and labeling ratio of monomeric actin. It contained 95 % unmodified actin and 5 % pyrene-labeled actin, at 23.8 μM total, corresponding to 5.95 x the final actin concentration for the pyrene assay, in G-buffer. In the cuvette, the actin premix was then diluted into Mg-G-buffer (5 mM TrisHCl pH 7.4, 0.2 mM $MgCl_2$, 1 mM DTT, and 0.2 mM MgATP) and allowed to incubate for 2 min. In this step, Ca^{2+} ions on actin monomers are exchanged for Mg^{2+} ions, ensuring that actin polymerization commences at a reproducible starting point. Salts, Arp2/3 and VCA were then added and mixed by pipetting 5 times. The cuvette was placed in the spectrophotometer and the measurement was started, noting down the delay between adding salt and the first recorded data point (usually 10-15 s). The measurement was left to run until the fluorescence intensity plateaued.

c. Data analysis While the Duetta spectrometer offers simultaneous buffer measurement and correction, we chose to perform a manual background correction to increase time resolution of our measurements. This allowed us to acquire one datapoint per 1.1 s. For every measurement day, we first performed blank measurements on F-buffer and F-buffer including 6.5 % optiprep, where we repeated the same measurement 20 times. We then averaged these data points for every buffer individually, and subtracted the average from the sample data before further processing. To extract the time it takes to reach maximum pyrene fluorescence, as well as the actin elongation rate at the time where half of all G-actin is polymerized, we use a custom-written python script following the analysis laid out in [9]. We extract the time it takes each sample to reach maximum pyrene fluorescence and hence steady-state actin polymerization, as well as the actin elongation speed at the inflection point of the pyrene fluorescence curve. At this point, it is assumed half of all actin has polymerized and the increase in fluorescence intensity is only due to elongation, not nucleation [9].

IV. SUPPLEMENTAL FIGURES

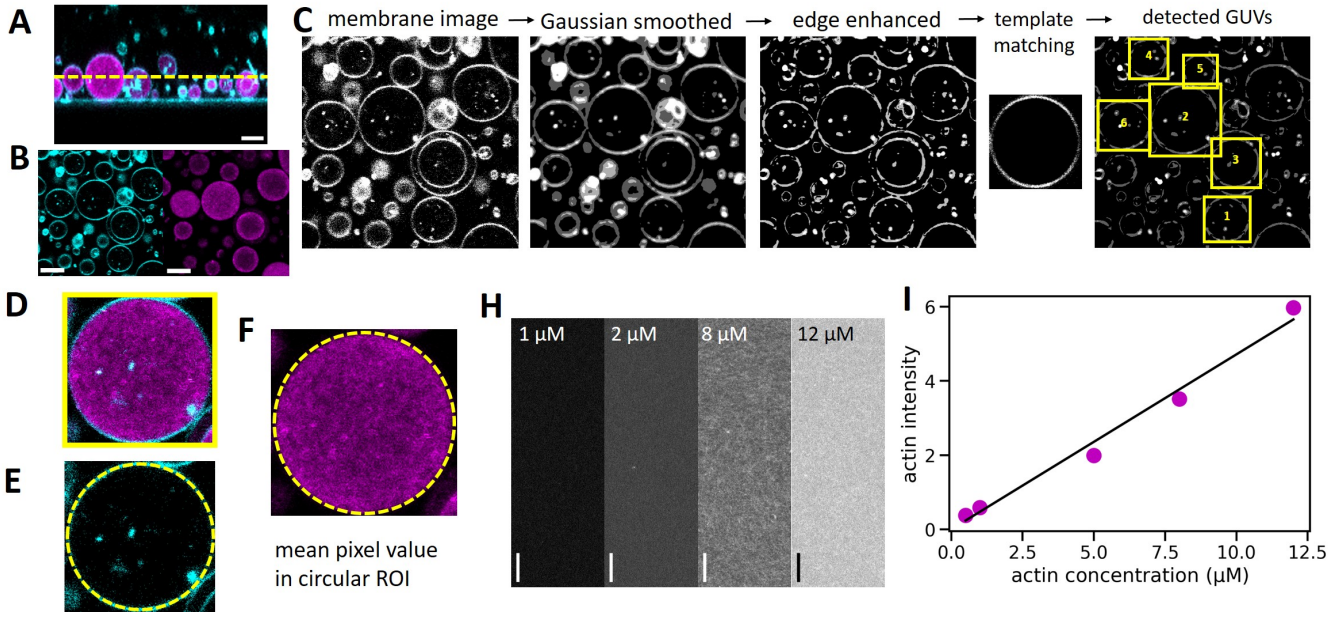

FIG. S4. **Quantifying actin concentrations.** (A) For quantitative confocal imaging, we performed an xz-scan to locate the precise z-position of the coverslip visible from its reflection (horizontal cyan line). Actin is shown in magenta, lipids in cyan. The yellow dashed line indicates a 7 μm height above the coverslip, where we took subsequent images. (B) Next, we acquired a two-channel xy-confocal image (actin in magenta, lipids in cyan). (C) We used an automated pipeline to detect the vesicles by pre-processing the images and subsequently locating GUVs using the template matching module in the DisGUVery toolbox [10]. Yellow boxes indicate the detected GUVs. (D) To extract the actin intensity inside a given GUV, we used the original unprocessed two-color image. We loaded each GUV detected by the template matching algorithm (here: GUV 2 from panel C) and drew a circular ROI of the same size as the template matching box ((E), yellow dashed circle). The mean pixel value inside this circular ROI in the actin channel was then taken as the average actin intensity of the GUV. To convert actin intensities into concentrations, we acquired a series of reference images of bulk actin networks (H) and constructed a concentration-intensity-calibration curve (I). Magenta datapoints represent the average mean pixel values of at least four 2048x2048 px reference images per condition, with standard deviations smaller than the data points. We fit the datapoints with a proportional model ($I_{\mathrm{act}}(c_{\mathrm{act}}) = A \cdot c_{\mathrm{act}}$, black line), which yields a proportionality constant of 0.471. Scale bars: 5 μm.

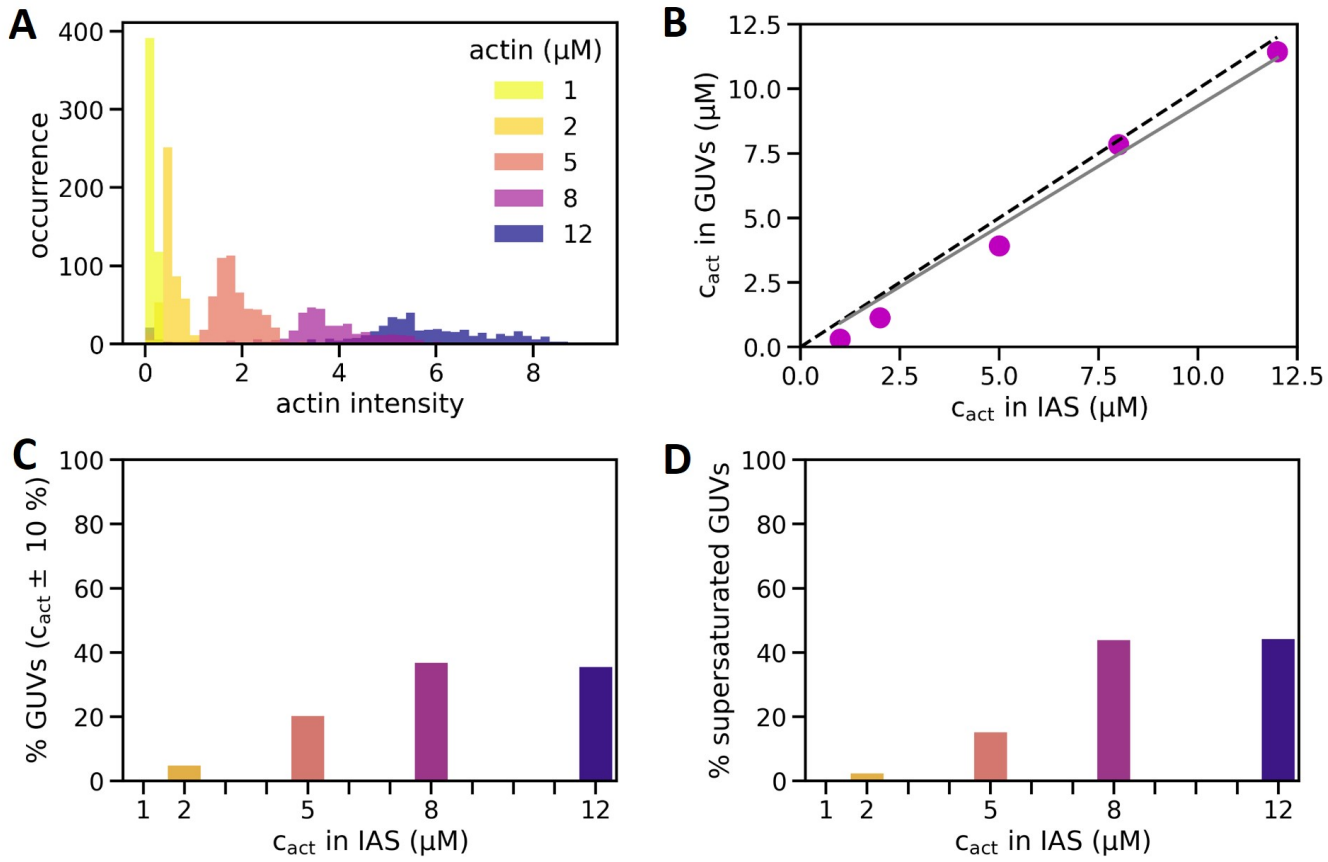

FIG. S5. **Extended quantification of actin encapsulation efficiency by eDICE.** (A) Histogram of actin intensities measured in individual GUVs by quantitative confocal microscopy. Darker colours indicate higher nominal actin concentrations. N = 2334 GUVs, with individual sample sizes N_i = 515, 468, 536, 368 and 447 GUVs for i = 1, 2, 5, 8, and 12 μM actin, respectively. (B) Mean actin concentration in the GUVs as a function of the nominal actin concentration in the inner aqueous solution. Magenta datapoints represent the mean of all GUVs at one nominal concentration (same sample sizes as in (A)), and the solid grey line indicates the proportional fit $c_{GUV}(c_{IAS}) = \xi \cdot c_{IAS}$, with $\xi = 93.3\%$. The dashed black line indicates perfect encapsulation, where the concentration in the GUVs equals the input concentration in the IAS. Error bars (95 % confidence interval on the mean) are not shown since they are smaller than the data points. (C) Bar plot showing the fraction of GUVs at different nominal actin concentrations containing actin at approximately the same concentration as the IAS (concentrations at $c_{nominal} \pm 10$ %). (D) Bar plot showing the fraction of GUVs that are significantly supersaturated in actin ($c_{GUV} > 1.1 \cdot c_{nominal}$).

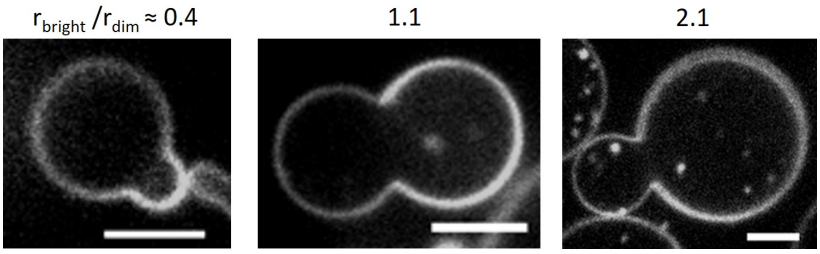

FIG. S6. **Dumbbell GUVs exhibit a range of shapes.** Most dumbbells had nearly equal sized lobes (middel panel, $r_{bright}/r_{dim} \approx 1$), but both significantly lower and higher size ratios also occurred (left and right panel, $r_{bright}/r_{dim} \approx 0.4$ and 2.1, respectively).

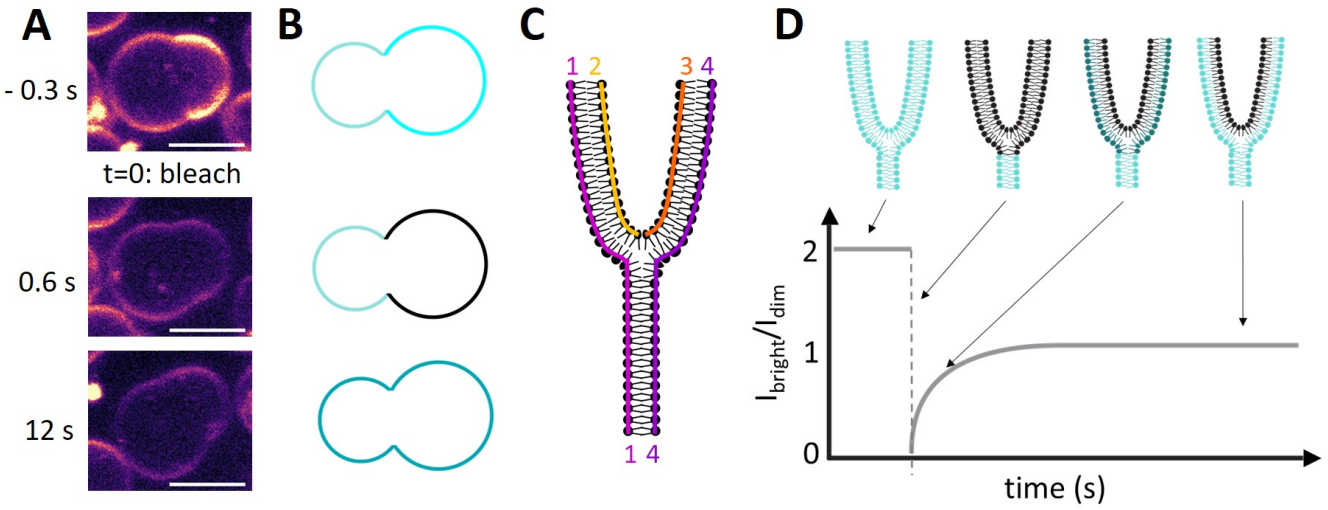

FIG. S7. **FRAP analysis to test a mechanism for dumbbell formation based on hemifusion of nested GUVs.** (A) Confocal images taken at the equatorial plane of a dumbbell-shaped GUV before and after bleaching the bright lobe. Scale bars: 5 μm. Membrane fluorescence is shown in false color (magma) for clarity. (B) Schematic of the bleaching experiment. The GUV starts out with a dim and a bright lobe (top). Ideally, all of the bright lobe's fluorescence gets bleached (middle). The remaining fluorescence from the unbleached lobe then redistributes in all connected leaflets of both lobes. (C) Schematic of the different lipid leaflets at the neck, assuming that the dumbbell shape results from hemifusion: leaflets 1 and 4 connect the dim and bright lobe, while leaflets 2 and 3 are disconnected and only span the bright lobe. Note that 'leaflets' 2 and 3 are two halves of one continuous monolayer of lipids that is bent in on itself, making it macroscopically appear as two separate leaflets. (D) Expected ideal recovery curve (bottom) and illustration of the fluorescence distribution in the different leaflets (top). Leaflets 2 and 3 (C) do not exchange lipids with leaflets 1 and 4, and consequently remain dark after bleaching. The intensity ratio between the bright and dim dumbbell lobes thus recovers not to 2, but to 1.

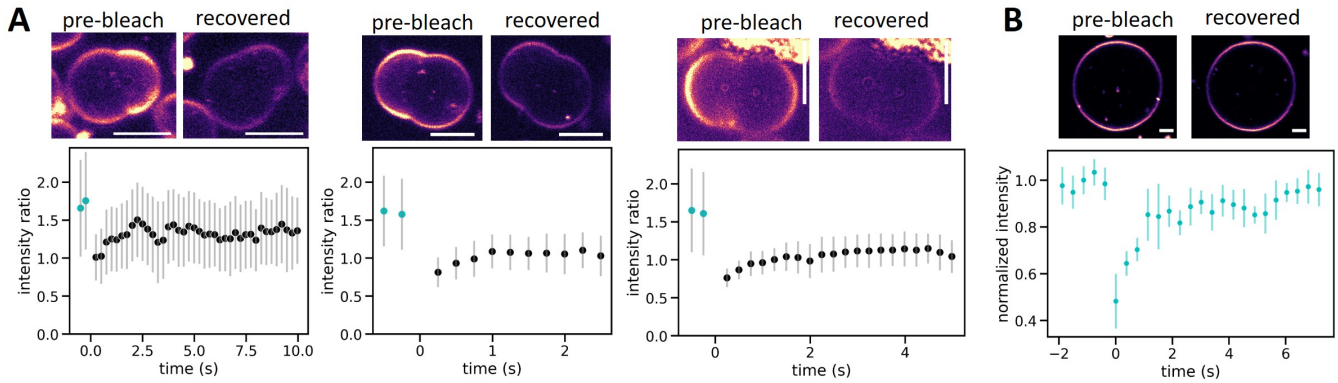

FIG. S8. **Extended FRAP data for dumbbell-shaped GUVs.** (A) Example FRAP curves for three additional dumbbells not shown in the main text. The bright lobe was bleached to approximately 30 % of its initial fluorescence intensity at t=0. The intensity ratio between the bright and the dim lobe consistently started out at around 1.7 (cyan data points), and recovered to between 1.0 and 1.4 within 2 s (black data points). (B) FRAP curve of a non-dumbbell GUV. Here, a 2x5 μm rectangular ROI at the top of the GUV was photobleached and the fluorescence recovery was monitored relative to a reference region on the opposite side of the GUV. The effect of photobleaching appeared more pronounced here than in the dumbbell GUVs, as we could bleach the small region much faster and were thus able to capture more of the initial recovery period. The fluorescence recovery timescale matched that seen in dumbbell GUVs (< 3 s). Confocal images above each graph show the equatorial slice of the GUV before photobleaching and after at least 15 s of recovery. Scale bars: 3 μm. Membrane fluorescence is shown in false color (magma) for clarity.

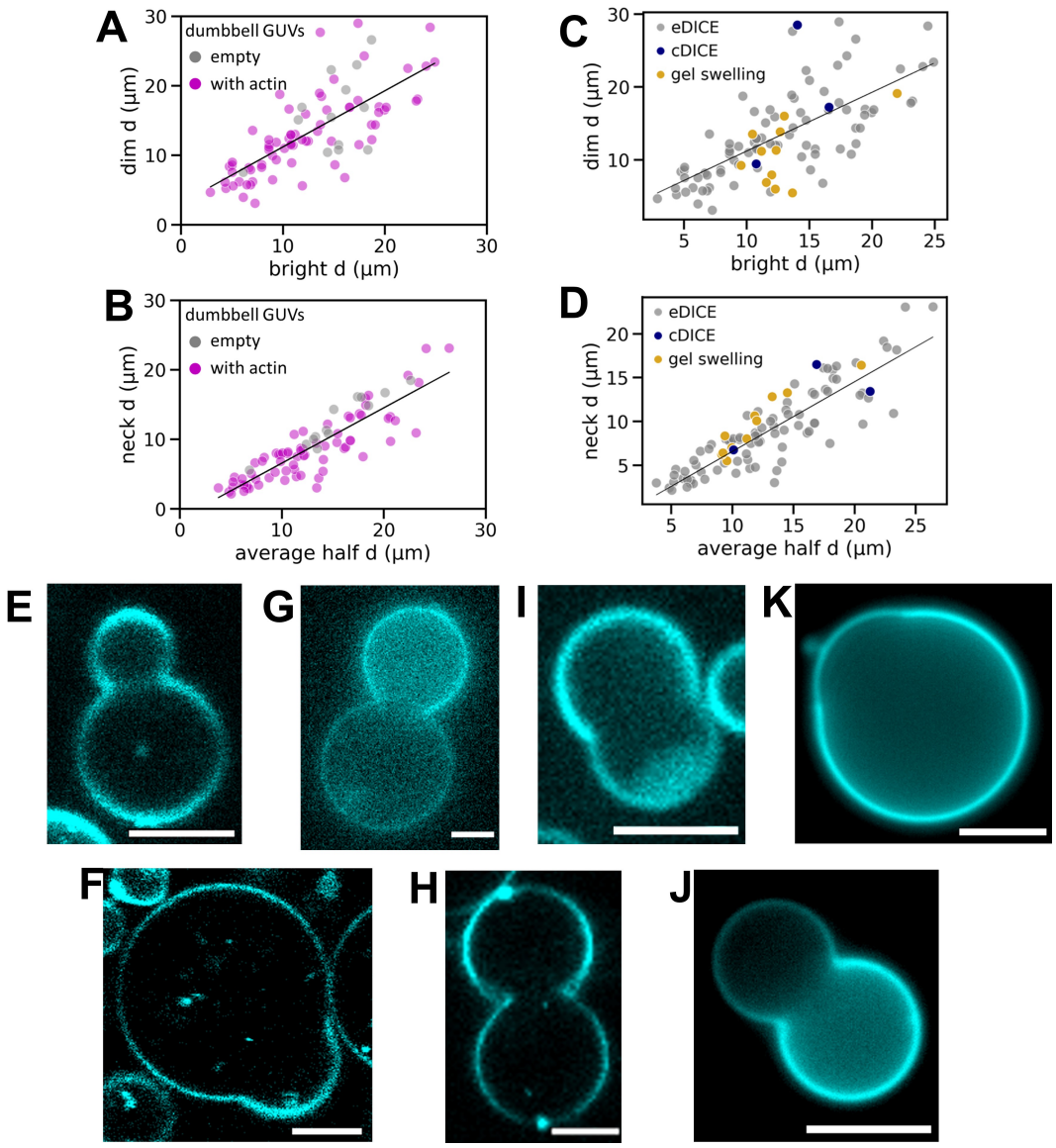

FIG. S9. **Dumbbell GUVs form for a range of IAS compositions and GUV production methods.** (A, B) Data from Fig. 4 H and I are re-plotted to show which dumbbells contain actin (magenta datapoints, either 4.4 or 8 μM actin in F-buffer, N = 72 GUVs) or only F-buffer (grey datapoints, N = 13). Actin does not appear to alter the formation of dumbbell shaped GUVs. (C, D) The shapes of dumbbells produced by cDICE (blue datapoints, N=3) and gel swelling (yellow datapoints, N=11) follow the same trends in relative lobe dimensions (C) and neck dimensions (D) as those produced by eDICE (grey datapoints, N=72). (E-L) Fluorescence microscopy images of dumbbell shaped GUVs produced in different circumstances. Dumbbells form in GUVs encapsulating only buffer (E), actin which polymerizes in the lumen without nucleating proteins (F), different concentrations of actin nucleated on the membrane by Arp2/3 and VCA (G: 4 μM actin, H: 8 μM actin), and with cortices where Arp2/3 driven actin nucleation is modulated by capping protein (I). (J) Dumbbell vesicles are also occasionally observed in samples produced by cDICE, in this case encapsulating G-buffer. (K) We even find dumbbells (albeit only rarely, < 2 %) when GUVs are produced by gel-assisted swelling and encapsulate only a sucrose solution. E, F, and H were acquired on a laser scanning confocal microscope; G and I were acquired on a spinning disk confocal microscope, and J and K were acquired on a Nikon epifluorescence microscope. Scale bars: 5 μm.

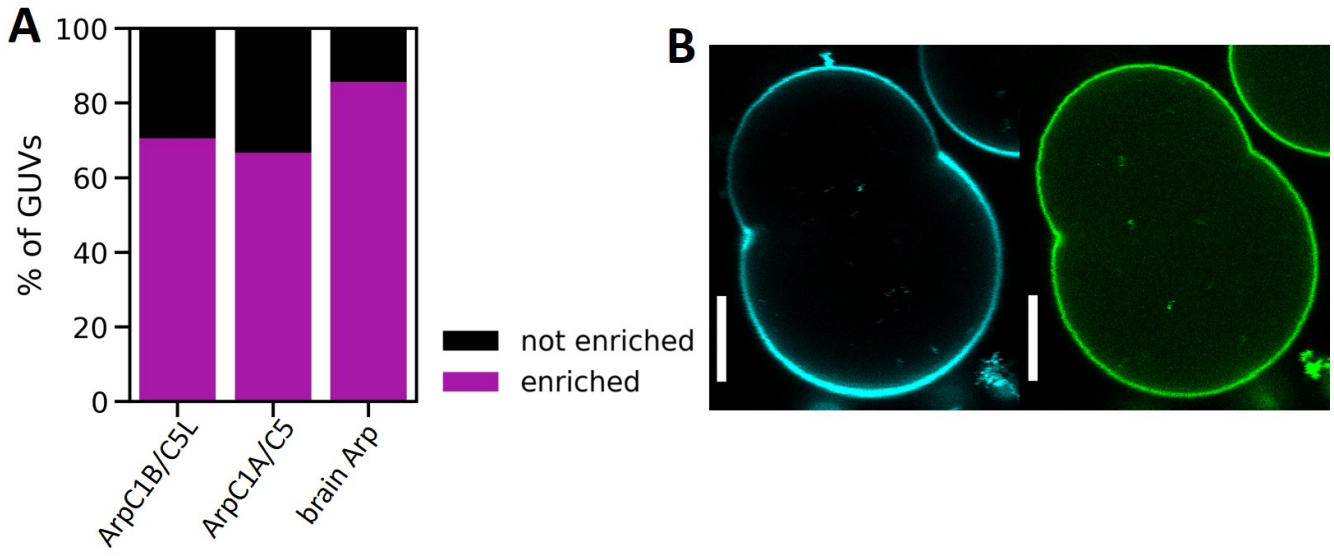

FIG. S10. **Actin was consistently enriched at the necks of dumbbell GUVs for different Arp2/3 isoforms, while VCA alone did not show enrichment.** (A) Bar plot showing the fraction of dumbbell GUVs in which actin was enriched at the neck, depending on the isoform of Arp2/3 which nucleates actin at the cortex. Actin and Arp2/3 were always at 8 μM and 50 nM, respectively, and VCA was either at 2 or 6.5 μM. Capping protein was absent. N = 17, 3 and 7 for Arp2/3 isoforms Arp2/3C1BC5L, Arp2/3C1AC5, and mixed isoforms isolated from porcine brain, respectively. While statistics for Arp2/3C1AC5 and brain Arp2/3are low, the data suggest that dendritic actin networks preferentially assemble at concave GUV neck regions for all these Arp2/3 isoforms. (B) Representative confocal image of a dumbbell GUV (membrane in cyan) encapsulating 6.5 μM fluorescent VCA (green). VCA covered the inner leaflet homogeneously, and we did not observe VCA enrichment at any of the 5 observed dumbbell necks.

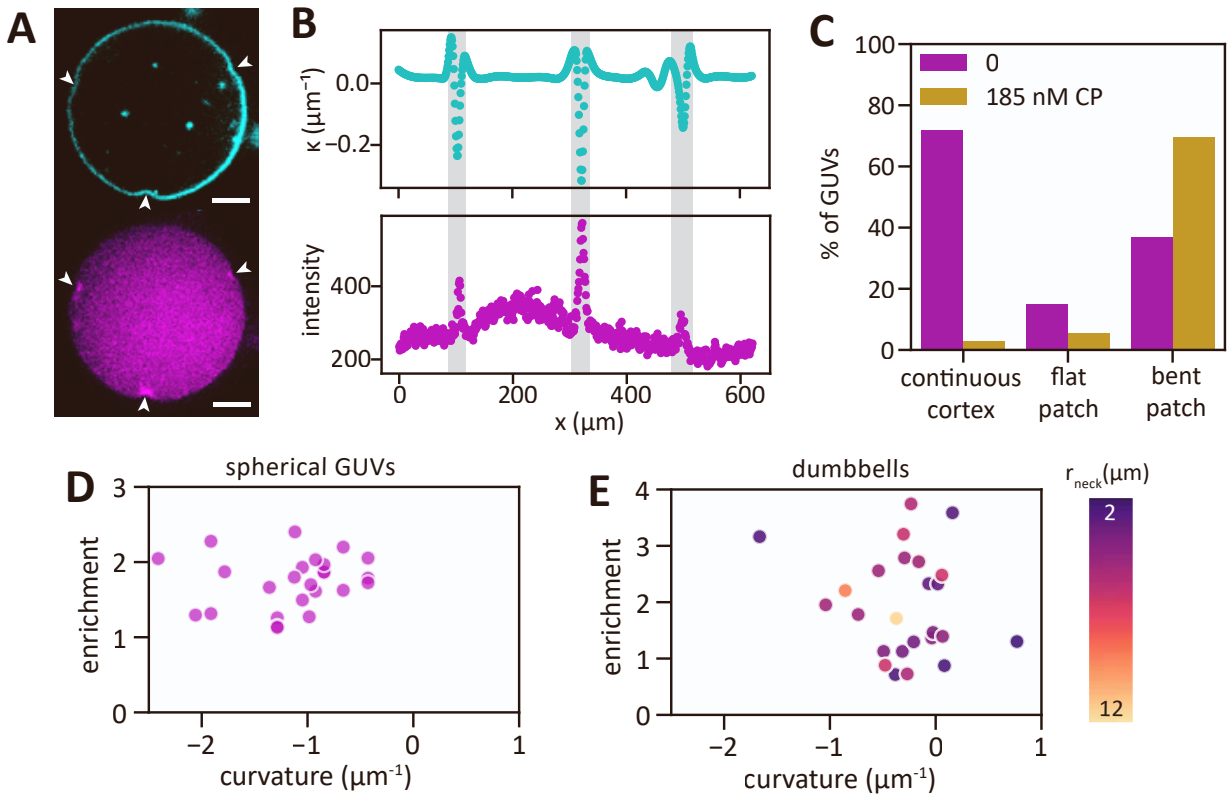

FIG. S11. **Branched actin networks associate with curved membrane regions in both spherical and dumbbell GUVs.** (A) Confocal slice of a GUV co-encapsulating 8 μM actin, 50 nM Arp2/3, 2.6 μM VCA and 185 nM capping protein. Actin (magenta) is enriched in small, bright, concave patches (white arrowheads) colocalized with bent sections of the GUV membrane (cyan). Scale bars: 5 μm. (B) Line profiles of the local membrane curvature (top) and actin signal intensity (bottom) along the GUV membrane in (A) confirm that spikes in actin signal occur at locations of negative membrane curvature (grey shaded regions). (C) Bar plot of the fraction of spherical GUVs with a continuous cortex, flat cortical patches, or bent cortical patches, for cortices without (magenta, N = 60 GUVs) or with (yellow, N = 36 GUVs) 185 nM capping protein. (D) Actin enrichment in bent patches as a function of patch curvature (N = 37 patches in 20 separate GUVs containing 185 nM capping protein). (E) Actin enrichment at dumbbell necks as a function of curvature. The data is color coded to reflect the 3D structure of the neck: darker colors indicate tighter necks with smaller r_{neck} (see color bar on the right). N = 27 dumbbell necks.

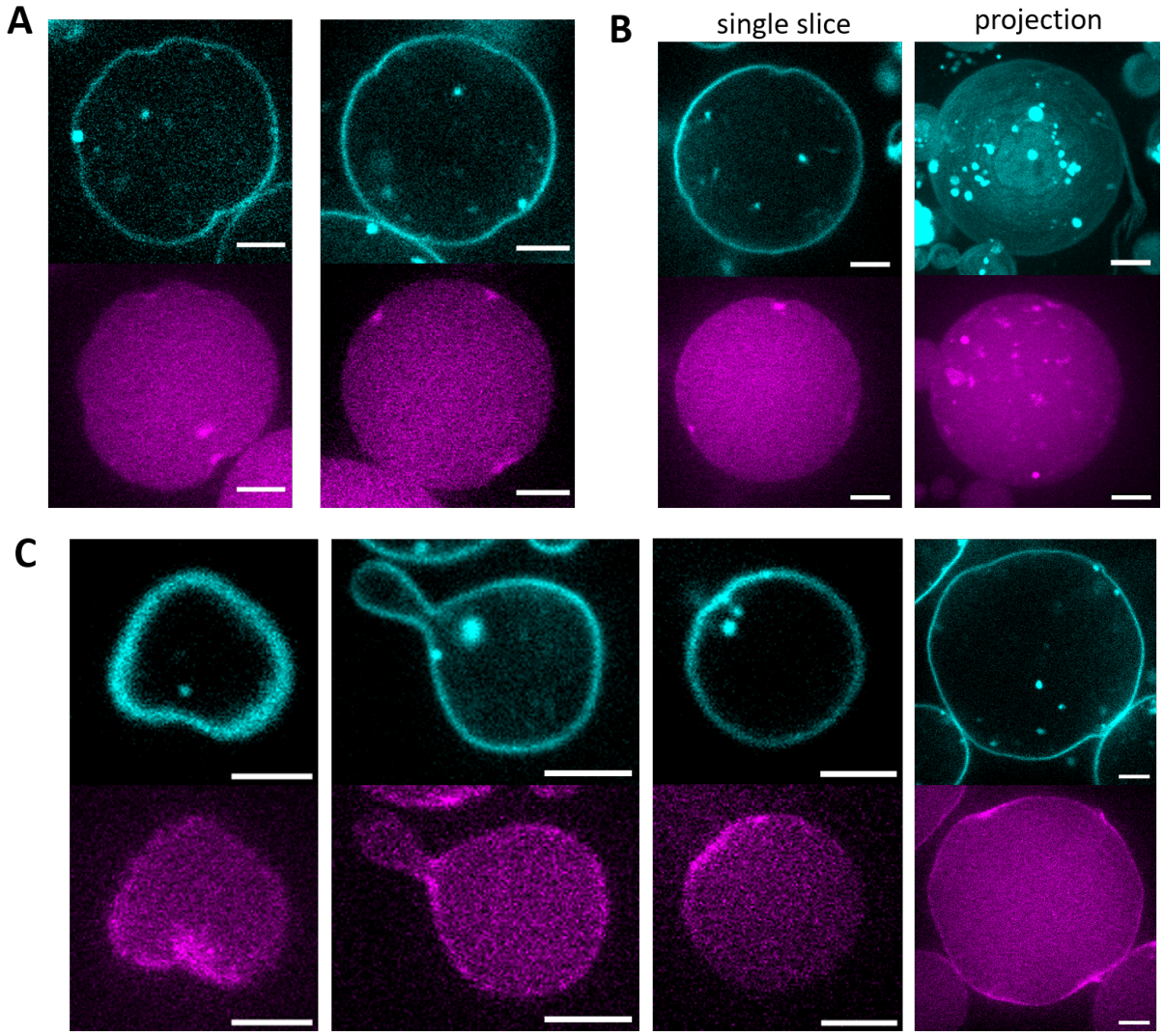

FIG. S12. **Concave actin patches in the presence of capping protein.** Confocal microscopy slices of two representative GUVs containing 8 μM actin, 50 nM Arp2/3 and 2.6 μM VCA, combined with 185 nM capping protein. Under these conditions, we observed small regions in which actin (magenta) was enriched at an inwardly bent membrane region (cyan). Typically, GUVs had a few (2-5) patches like the two examples shown in (A), but they could also bear many more concave patches spaced all around the GUV (B). The left and right panels in (B) show a single confocal slice and a maximum intensity projection of the same GUV, and all bright spots visible in the projection represent concave patches. (C) Confocal slices of GUVs with bent actin patches in GUVs with 8 µM actin, but no capping protein. Scale bars: 5 μm.

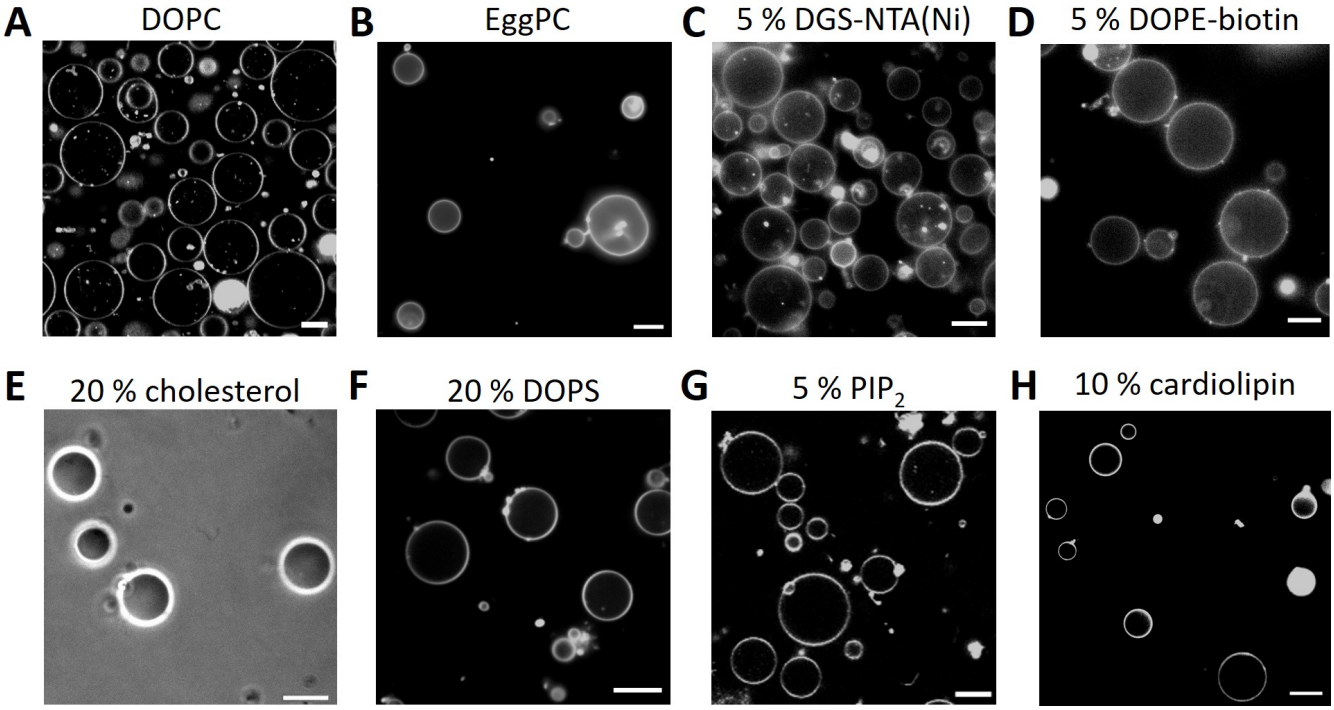

FIG. S13. **eDICE successfully produces GUVs with different lipid compositions.** (A) DOPC, (B) EggPC, (C) 95 % DOPC and 5 % DGS-NTA(Ni), (D) 95 % DOPC and 5 % biotin-DOPE, (E) 80 % DOPC and 20 % cholesterol, (F) 80 % DOPC and 20 % DOPS, (G) 95 % DOPC and 5 % PIP2, (H) 90 % DOPC and 10 % cardiolipin. (A) and (G) are confocal images acquired on the Stellaris LSCM, (B)-(D) and (H) are epifluorescence images acquired on the Nikon epifluorescence microscope, (E) was acquired on the same Nikon microscope in phase contrast mode, and (F) is a confocal image taken on the spinning disk confocal microscope. All GUVs except those shown in (E) are labeled with either 0.005 or 0.05 % of Cy5-DOPE. Scale bars: 10 μm.

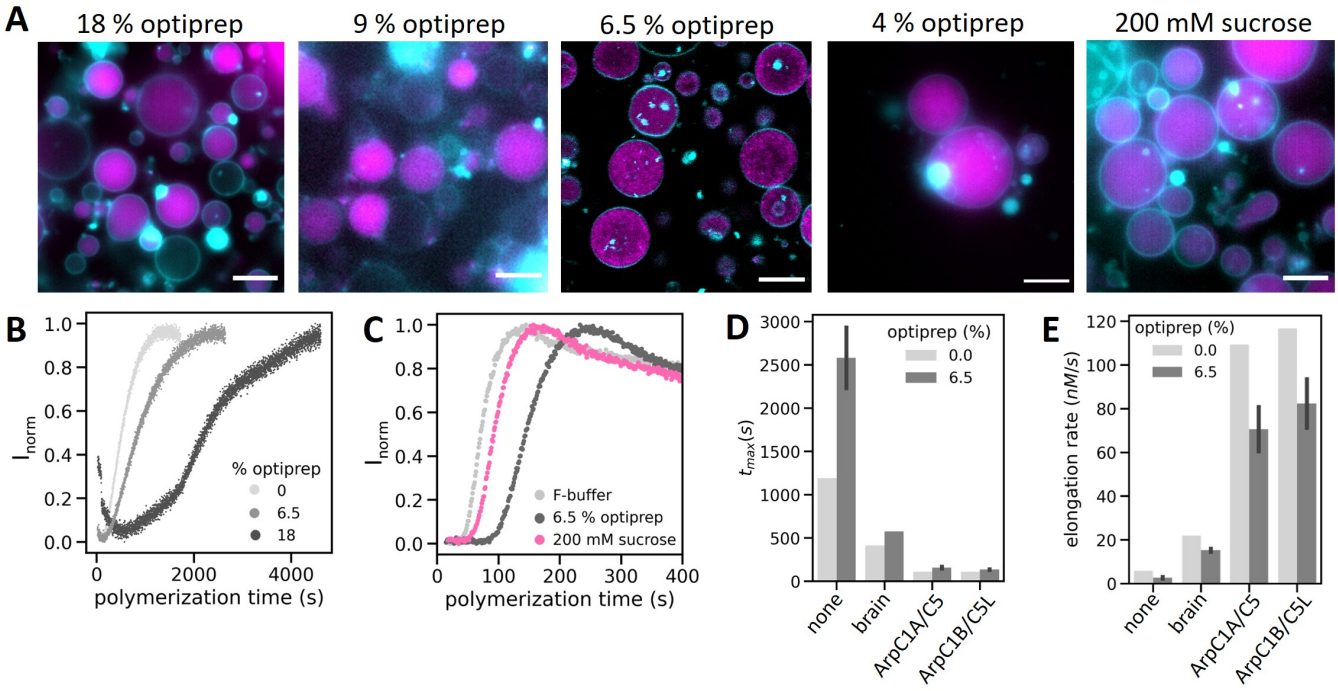

FIG. S14. **Effect of density gradient media on actin encapsulation and polymerization.** (A) Fluorescence images of GUVs encapsulating F-actin using different concentrations of density gradient media (see legends) in the IAS. The GUVs containing 6.5 % optiprep are shown as a single confocal slice, the other images show widefield images. Lipids are shown in cyan, actin in magenta. Scale bars: 10 μm. (B) Actin polymerization curves measured by pyrene fluorescence assay at different concentrations of Optiprep showed that optiprep interferes significantly with actin polymerization. (C) Pyrene actin polymerization curves indicate that sucrose used at a concentration compatible with eDICE also slowed actin polymerization dynamics, but to a lesser degree than Optiprep. (D) Bar plot of the time to reach steady state, $t_{\max}$ in the presence and absence of 6.5 % optiprep. (E) Bar plot of the actin elongation rate. Light grey bars in panels D and E represent one measurement in F-buffer, and dark grey bars represent the means of at least two separate measurements in F-buffer with optiprep, with error bars indicating the full spread of the data.

V. SUPPLEMENTAL TABLES

Compound	Instrument	Excitation	Detection
actin-AF488	Olympus spinning disk	491 nm laser, 10.5 %, 200 ms	Andor iXon X3 EM-CCD, gain 250
membrane-Cy5	Olympus spinning disk	640 nm laser, 53 %, 200 ms	Andor iXon X3 EM-CCD, gain 250
actin-AF488	Leica Stellaris LSCM	WLL at 499 nm, 18 %, 3.16 µs dwell time	HyDS2 (504-590 nm), counting mode
membrane-Cy5	Leica Stellaris LSCM	WLL at 640 nm, 2 %, 3.16 µs dwell time	HyDX3 (658-809 nm), counting mode
VCA-AF488C5	Leica Stellaris LSCM	WLL at 499 nm, 2 %, 3.16 µs dwell time	HyDX1 (510-567 nm), Standard mode, gain 60
actin-AF488	Nikon widefield	470 nm LED, 25 %, 200 ms	Hamamatsu Orca Flash 4.0
membrane-Cy5	Nikon widefield	640 nm LED, 30 %, 50 ms	Hamamatsu Orca Flash 4.0
actin-AF488	Leica widefield	475 nm LED, 5 %, 200 ms	sCMOS camera, gain 2
membrane-Cy5	Leica widefield	635 nm LED, 5 %, 50 ms	sCMOS camera, gain 2

TABLE S1. List of imaging settings. The left column lists the compound and their label, which is Alexa Fluor 488 (AF488) or Cy5. The 'Excitation' column shows the excitation wavelength, laser attenuation, and exposure time (camera-based microscopes) or pixel dwell time (confocal scanning microscope).

SUPPORTING REFERENCES

[1] F. Jülicher and R. Lipowsky, Domain-induced budding of vesicles, Physical Review Letters **70**, 2964 (1993).

[2] F. Julicher and R. Lipowsky, Shape transformations of vesicles with intramembrane domains, Physical Review E **53**, 2670 (1996).

[3] T. Baumgart, S. T. Hess, and W. W. Webb, Imaging coexisting fluid domains in biomembrane models coupling curvature and line tension, Nature **425**, 821 (2003).

[4] J. M. Allain and M. B. Amar, Budding and fission of a multiphase vesicle, European Physical Journal E **20**, 409 (2006).

[5] T. Baumgart, S. Das, W. W. Webb, and J. T. Jenkins, Membrane elasticity in giant vesicles with fluid phase coexistence, Biophysical Journal **89**, 1067 (2005).

[6] A. Weinberger, F. C. Tsai, G. H. Koenderink, T. F. Schmidt, R. Itri, W. Meier, T. Schmatko, A. Schröder, and C. Marques, Gel-assisted formation of giant unilamellar vesicles, Biophysical Journal **105**, 154 (2013).

[7] L. V. D. Cauter, F. Fanalista, L. V. Buren, N. D. Franceschi, E. Godino, S. Bouw, C. Danelon, C. Dekker, G. H. Koenderink, and K. A. Ganzinger, Optimized cdice for efficient reconstitution of biological systems in giant unilamellar vesicles, ACS Synthetic Biology **10**, 1690 (2021).

[8] J. A. Cooper, S. B. Walker, and T. D. Pollard, Pyrene actin: documentation of the validity of a sensitive assay for actin polymerization, Journal of Muscle Research and Cell Motility **4**, 253 (1983).

[9] L. K. Doolittle, M. K. Rosen, and S. B. Padrick, Measurement and analysis of in vitro actin polymerization, in *Adhesion Protein Protocols*, edited by A. S. Coutts (Humana Press, 2013) pp. 273–293.

[10] L. van Buren, G. H. Koenderink, and C. Martinez-Torres, Disguvery: A versatile open-source software for high-throughput image analysis of giant unilamellar vesicles, ACS Synthetic Biology **12**, 120 (2023).